J. Fluid Mech. (2005), *vol.* 542, *pp.* 251–279.
doi:10.1017/S0022112005006336 Printed in the United Kingdom

Rayleigh–Taylor instability in complex stratifications

By J. W. JACOBS[1] AND S. B. DALZIEL[2]

[1]Department of Aerospace and Mechanical Engineering, University of Arizona, Tucson, AZ 85721, USA

[2]Department of Applied Mathematics and Theoretical Physics, University of Cambridge, Wilberforce Road, Cambridge CB3 0WA, UK

(Received 15 January 2003 and in revised form 2 June 2005)

The Rayleigh–Taylor instability of a system of three fluids separated by one unstable and one stable interface has been investigated experimentally. The experiments were gravitationally driven and conducted with miscible liquids consisting of salt solutions and fresh water. The lower two layers are initially gravitationally stable and are formed by depositing the lighter fluid on top of a thicker layer of the heavier one. The relatively thick top layer is initially separated from the two lower layers by a rigid barrier that is removed at the start of an experiment. In situations where the density of the bottom-layer fluid equals that of the top-layer fluid, the resulting turbulent flow is found to be self-similar as demonstrated by the collapse of the mean concentration distributions as well as the behaviour of the decay of the peak of the mean concentration profiles. In this configuration, the erosion of the bottom layer by the turbulence generated by the upper unstable interface is found to be small. When the density of the bottom-layer fluid is increased above that of the top-layer fluid, the degree of erosion is further decreased. In the cases where the lower interface is stably stratified at late-time, the entrainment rate E at the lower (statically stable) interface is found to follow a power law of the Richardson number, i.e. $E \propto Ri^{-n}$, with $n \approx 1.3$, a result in agreement with studies of mixing induced by oscillating grids. When the density of the bottom-layer fluid is decreased below that of the top-layer fluid, the erosion increases as expected. However, in this case, the overall density distribution is such that it is globally Rayleigh–Taylor unstable at late time. In this situation, the turbulent mixing region at late times grows similarly to that of single-interface Rayleigh–Taylor instability with approximately the same value of the growth constant. In these late-time unstable experiments the density profile approaches that of an equivalent two-layer Rayleigh–Taylor unstable system.

1. Introduction

Rayleigh–Taylor (RT) instability plays a fundamental role in the mixing processes of many stratified flows. In its simplest form, RT instability is produced by accelerating a density interface in the direction of its normal. If the direction of acceleration is from the lighter fluid into the heavier one, small perturbations on the nominally planar interface will grow and ultimately develop into a turbulent flow. Rayleigh–Taylor-generated turbulence has important consequences in astrophysical, geophysical and technological applications. A technological application of particular current importance is inertial confinement fusion (ICF), in which the turbulence generated by RT instability is detrimental. As a result, the presence of RT mixing has delayed the achievement of a productive fusion reaction.

Rayleigh (1900) was the first to analyse Rayleigh–Taylor instability in the context of an unstable stratification in a gravitational field. Later, Taylor (1950) considered the growth of perturbations to a flat interface separating two fluids of unequal densities when subject to an acceleration. Since then, Rayleigh–Taylor instability has received considerable attention in the form of analytical, numerical and experimental research. A comprehensive review of early work is given by Sharp (1984) and more recent work is summarized by Dimonte *et al.* (2004). Most of this work has been confined to the simplest possible case: two layers of uniform density and approximately equal depth.

This standard Rayleigh–Taylor instability has a number of key characteristics. If the instability grows from a single mode disturbance, the initial linear phase of growth is exponential, but this saturates as the flow becomes nonlinear, leading to a linear growth at later times. In contrast, naturally occurring instabilities develop from a range of wavelengths that interact and grow as the instability develops. This continual growth leads to the development of a self-similar character, where the dominant wavelength scales with the width of the developing mixing zone. Experimental evidence suggests that the half width δ, of the mean concentration profile grows as $\delta = \alpha A g t^2$, where $A = (\rho_1 - \rho_2)/(\rho_1 + \rho_2)$ is the Atwood number (ρ_1 and ρ_2 are the density of the upper and lower layers, respectively), g is the driving acceleration, and α is a dimensionless constant. This relationship is borne out by both experiments and numerics, although there has been a long debate on the precise value of the constant of proportionality α. Dimonte *et al.* (2004) summarize the values of α obtained by a large number of experimental and computational studies. Recent work (e.g. Dalziel, Linden & Youngs 1999; Cook & Dimotakis 2001) shows that the growth rate constant α depends not only on the density contrast, but also on the structure of the initial conditions. Although the high wavenumber modes are the most unstable in the linear phase, their growth rate saturates earlier, with further development of the t^2 growth relying on the lower wavenumber modes. If these lower wavenumber modes are present in the initial conditions they develop more quickly and begin to dominate the growth earlier (and hence yield a faster growth) than if the modes have to develop purely from the nonlinear interaction of high-wavenumber modes. In either case, as the instability develops, the high-wavenumber spectrum tends towards a self-similar cascade (Dalziel *et al.* 1999), with the density field adopting a fractal structure.

This paper presents experiments of flows one level greater in complexity than the standard two-layer instability. In particular, we investigate the effect of introducing a third layer to the problem, but restrict ourselves to the Boussinesq limit where the density differences are small compared to the densities themselves. In this limit, the density differences are important only when multiplied by the driving acceleration, g. The densities of the three layers, ρ_1, ρ_2 and ρ_3 as shown in figure 1, are chosen so that the upper interface is statically unstable (i.e. $\rho_1 > \rho_2$) and the lower interface is statically stable with $\rho_2 < \rho_3$. From these three densities we may define two independent dimensionless quantities analogous to the two-layer Atwood number: $A_{12} = (\rho_1 - \rho_2)/(\rho_1 + \rho_2)$ and $A_{13} = (\rho_1 - \rho_3)/(\rho_1 + \rho_3)$. In addition, it is useful to introduce the dimensionless time $\tau_{12} = (A_{12} g / h_2)^{1/2} t$. For this paper we restrict ourselves to $A_{12} > 0$ since the upper interface is always statically unstable, and $A_{13} < A_{12}$ since we have a Boussinesq system and the lower interface is always statically stable. Thus the experiments begin with the RT instability of only the upper interface until $\tau_{12} = O(1)$, when it begins to interact with the lower interface. To understand the development of the flow after this time also requires a knowledge of the relationship between ρ_1 and ρ_3 (or A_{13}) and the depth (or thickness) of the middle layer. We will consider

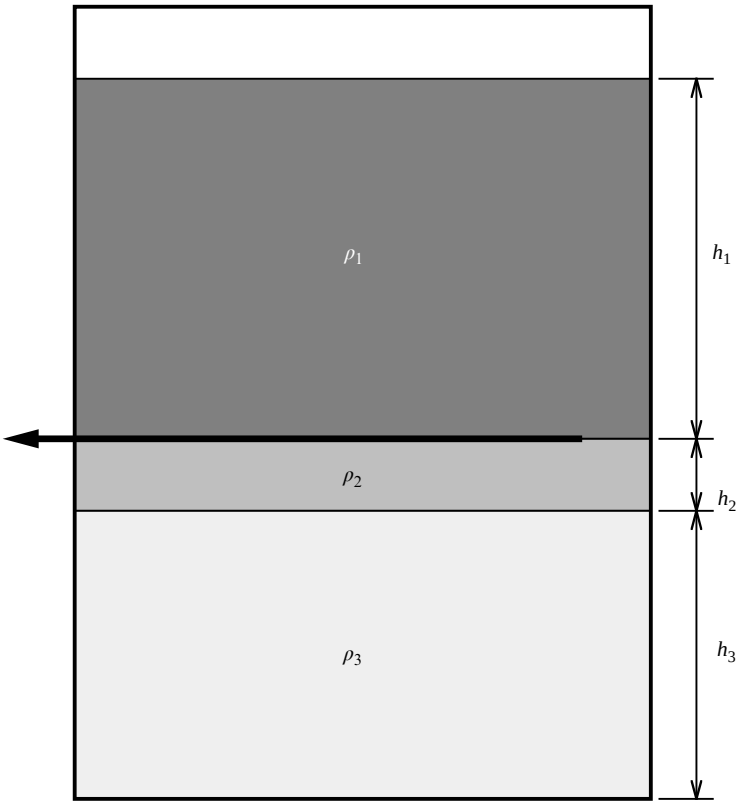

FIGURE 1. Schematic of the experimental apparatus.

cases where the flow is *globally stable* with $A_{13} < 0$, *globally neutral* with $A_{13} = 0$, and *globally unstable* with $A_{13} > 0$.

The introduction of the lower locally stable interface changes the problem of Rayleigh–Taylor instability to a combined problem where the kinetic energy produced by the Rayleigh–Taylor instability in turn drives a turbulent entrainment across the lower stable interface. Most previous work on mixing across an interface has fallen into one of two categories: internal mixing, where energy is extracted from a mean shear flow through Kelvin–Helmholtz and Hölmböe instabilities (e.g. Strang & Fernando 2001), or external mixing, where the source of turbulence is remote from the interface (e.g. Nokes 1988). The mixing produced by Rayleigh–Taylor instability interacting with the stable interface includes elements of both of these. It also has some of the characteristics of the mixing produced by buoyant plumes interacting with an interface (e.g. Baines 1975; Kumagai 1984), but unlike the plume, it acts in a statistically uniform manner over the entire surface of the interface. In cases when the bottom layer is denser than the top layer (or indeed of the same density), then we may anticipate that the entrainment across the interface will be more similar to that of external mixing.

Although much progress has been made in quantifying external mixing, it has become clear that the mixing efficiency (the ratio of the energy lost to mixing to the energy provided to the system) depends not only on the Richardson number of the flow, but also on the method by which energy is supplied to the flow (Balmforth, Llewellyn

Smith & Young 1998). In most cases, the mixing efficiency is seen to decrease at high stabilities (Richardson numbers), leading to a sharpening of interfaces and the formation of layers from an initially smooth density profile (e.g. Holford & Linden 1999); in some cases, the mixing efficiency plateaus but does not decrease (e.g. Higginson 2000). Other apparent inconsistencies include the dependence of the entrainment rate on the Schmidt number $Sc = \nu/\kappa$, with entrainment rates decreasing more rapidly with increasing Richardson number for higher Schmidt numbers. This investigation therefore is interesting not only in the context of Rayleigh–Taylor instability, but also in that it investigates the mixing induced by an energy source not previously considered.

For the present paper, we restrict our attention to the case where the thickness of the middle layer is much less than that of the top layer. In this case the mixed zone will continue to grow upwards, away from the initial location of the unstable interface, well after it begins to interact with the initially stable interface. Our experiments are designed to illuminate the basic dynamics of the flow and the resultant changes in the mean density profile. We explore the self-similar development of the mixing zone, and demonstrate that this is reflected by self-similarity in the entrainment across the lower, initially stable interface.

2. Experimental details

The experiments were conducted using the apparatus employed by Dalziel *et al.* (1999) in their study of single-interface Rayleigh–Taylor instability. This apparatus, which was derived from that used by Linden & Redondo (1991) and Linden, Redondo & Youngs (1994), consists of a rectangular acrylic tank measuring 40 cm in length, 20 cm in width and 60 cm in height (the vertical dimension) and is filled to a height of approximately 50 cm. Slots have been machined into the sides of the tank to allow the insertion of a horizontal barrier along the length of the tank at a height of 25 cm above the bottom. The apparatus uses the novel barrier design described in Dalziel *et al.* (1999) which minimizes the disturbance produced by the removal of the barrier. The barrier consists of a flat rigid tube made of stainless steel through which two pieces of nylon fabric are passed. Each piece is stretched through the tube and is attached to the endwall such that they line the upper and lower surfaces of the barrier. As the plate is removed, the nylon is pulled through the tube. Thus, the fabric lining remains stationary as the plate is removed, and therefore the upper and lower surfaces impart no shear stress to the fluids.

Prior to the start of an experiment, the volume below the barrier is partially filled to a height h_3 with a fluid of density ρ_3. The remaining height (h_2) below the barrier is then carefully filled with a fluid of lower density ρ_2 using a floating foam diffuser. After inserting the barrier, the remaining height (h_1) is filled with fluid of density ρ_1. The fluids consisted of salt (NaCl) solutions or fresh water with alcohol (isopropyl) added to match the index of refraction of all the layers (as described in Dalziel *et al.* 1999). In all the experiments, the Atwood number of the upper interface was $A_{12} = (\rho_1 - \rho_2)/(\rho_1 + \rho_2)$ kept constant at 0.0021, while the overall Atwood number $A_{13} = (\rho_1 - \rho_3)/(\rho_1 + \rho_3)$ was varied from -0.0021 to 0.0016. Given the Atwood number independence of RT instability in the Boussinesq limit, it is more convenient to refer to the Atwood number ratio $B = A_{13}/A_{12} \approx (\rho_1 - \rho_3)/(\rho_1 - \rho_2)$. Thus, B was varied from -1 to 0.75 in the experiments. The initial densities of the three layers were measured using a Paar densitometer to determine the Atwood number, which was found to be repeatable to within 5%. The solutions were preconditioned by exposing

them to a 300 mbar vacuum overnight to allow them to reach thermal equilibrium and remove most of the dissolved air. This was found necessary to prevent a plume of bubbles from forming at the trailing edge of the barrier during the removal process. Experiments were conducted with middle-layer thicknesses of 2.5, 5.0 and 7.5 cm, thus keeping $h_2 \ll h_1$.

An experiment is initiated by removing the barrier which separates the Rayleigh–Taylor unstable interface between fluids 1 and 2. The barrier is withdrawn manually by pulling on the nylon fabric passing through the length of the barrier while simultaneously pushing inward on the outer end of the barrier. The mean value of the withdrawal time for all of the experiments here was 2.5 s with a standard deviation of 0.28 s. A thorough discussion of the initial perturbation produced by the barrier removal including the effects of withdrawal speed can be found in Dalziel (1994).

The experiments were visualized using the planar fluorescence technique described by Dalziel *et al.* (1999). Fluorescein dye was initially added to one of the three layers at a 1×10^{-7} g l^{-1} concentration. The fluids were then illuminated using a 300 W xenon arc lamp that was positioned approximately 2.5 m from the tank. The light from the arc lamp was reflected from a front-silvered mirror to pass upward through a slit positioned at the bottom of the tank yielding a 2 mm thick light sheet that passed through the centre of the tank. The resulting fluorescent images were viewed by a monochrome CCD camera and recorded with a Super VHS video tape recorder. The stored images were later digitized to a resolution of 512×512 8-bit pixels and corrected for non-uniformity and absorption of the illuminating light sheet using the DigImage image processing software (see Dalziel *et al.* 1999).

3. Results and discussion

3.1. *Qualitative observations*

Figure 2 is a sequence of fluorescent images showing the development of the instability for a typical $B = 0$ experiment (i.e. $\rho_1 = \rho_3$) where the middle layer with initial thickness $h_2 = 5.0$ cm has been made visible by the addition of fluorescent dye. We can observe in the first few images of this sequence the growth of Rayleigh–Taylor instability on the upper unstable interface. Notice that this initial instability develops in a similar fashion to that of the earlier two-fluid experiments of Dalziel *et al.* (1999), i.e. the instability develops more quickly on the right-hand side of the tank owing to the finite withdrawal rate and finite volume of the barrier. In addition, a plume of heavy fluid is observed to quickly form and fall near the right-hand wall. However, when this plume impacts the lower stable interface, its development is halted. Thus, the late-time left-to-right asymmetry of these experiments is much less pronounced than it is in the single-interface experiments. The lower front of the mixing zone grows until it impacts the lower interface where its growth is halted. However, the turbulence generated by the instability is able to deform the interface as well as transport some of the bottom-layer fluid upward. Conversely, the upper portion of the mixing zone grows undisturbed until it reaches the top of the tank. Because there is a small finite amount of dye in the tank, the overall concentration is observed to decrease noticeably with time as the thickness of the layer increases.

Figure 3 is a sequence taken from a similar $B = 0$ experiment, but with the fluorescent dye initially mixed with the bottom-layer fluid. Note that the times of these images are different than those of figure 2. The sequences in which the dye is placed in the bottom layer end at $\tau_{12} = 12.84$ (20 s), instead of at $\tau_{12} = 7.70$ (12 s) as was the case for the sequence with the middle layer dyed. In this sequence, we can more easily observe the

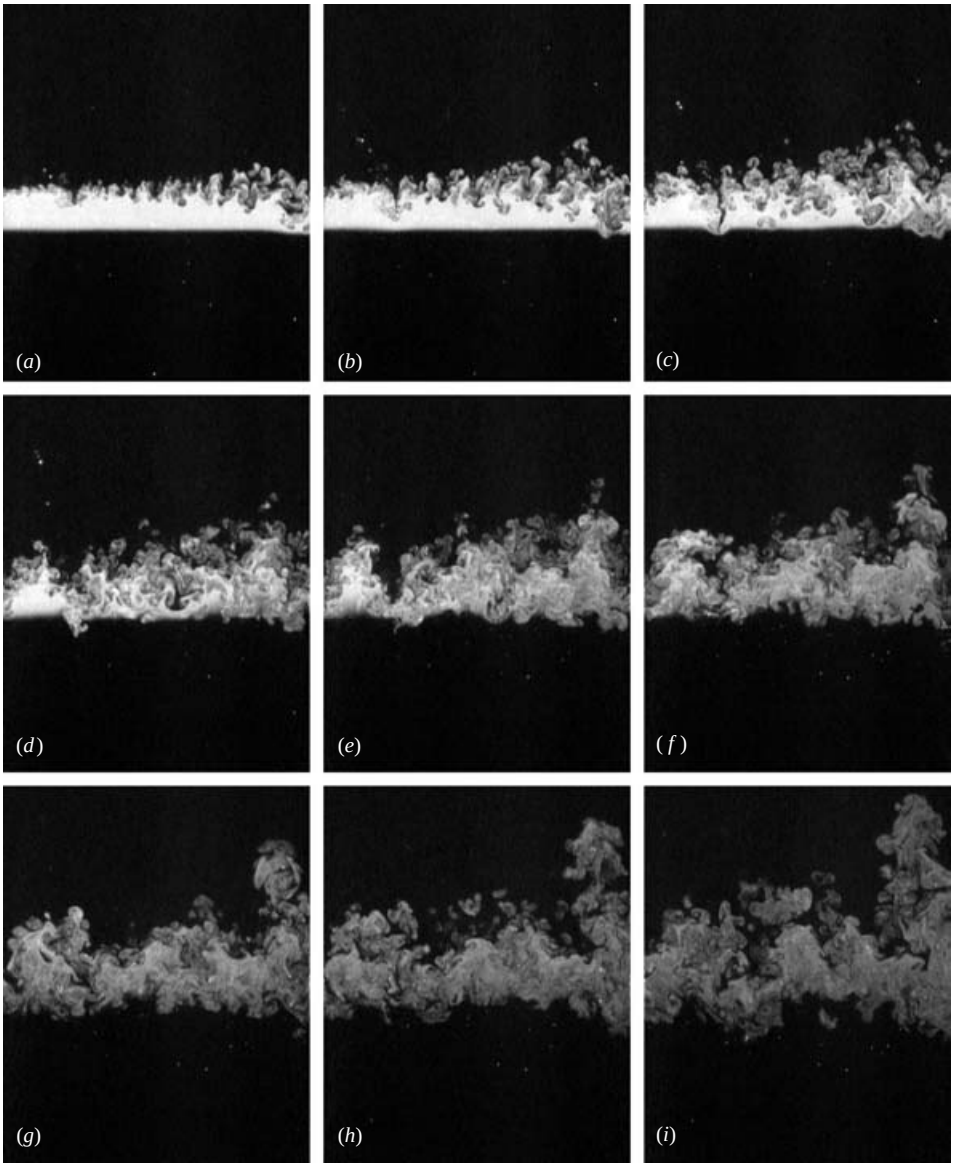

FIGURE 2. A sequence of light induced fluorescence (LIF) images showing the development of the instability for a typical $B = 0$ experiment (i.e. $\rho_1 = \rho_3$) where the middle layer with $h_2 = 5.0$ cm has been made visible by the addition of fluorescent dye. Dimensionless times (τ_{12}) relative to the start of the barrier removal are: (*a*) 1.54, (*b*) 2.31, (*c*) 3.08, (*d*) 3.85, (*e*) 4.62, (*f*) 5.39, (*g*) 6.16, (*h*) 6.93, (*i*) 7.70.

deformation of the lower interface produced by the still developing Rayleigh–Taylor instability of the middle layer. Note that the middle-layer fluid immediately above the lower interface will always be slightly less dense than the bottom-layer fluid, even if the fluid initially came from the top layer. Thus, hydrostatic forces will always act to stabilize the lower interface. Nevertheless, the turbulence of the middle region is sufficiently intense to significantly deform the interface. In addition, the turbulent action is able to entrain some of the bottom-layer fluid, which is easily observed in

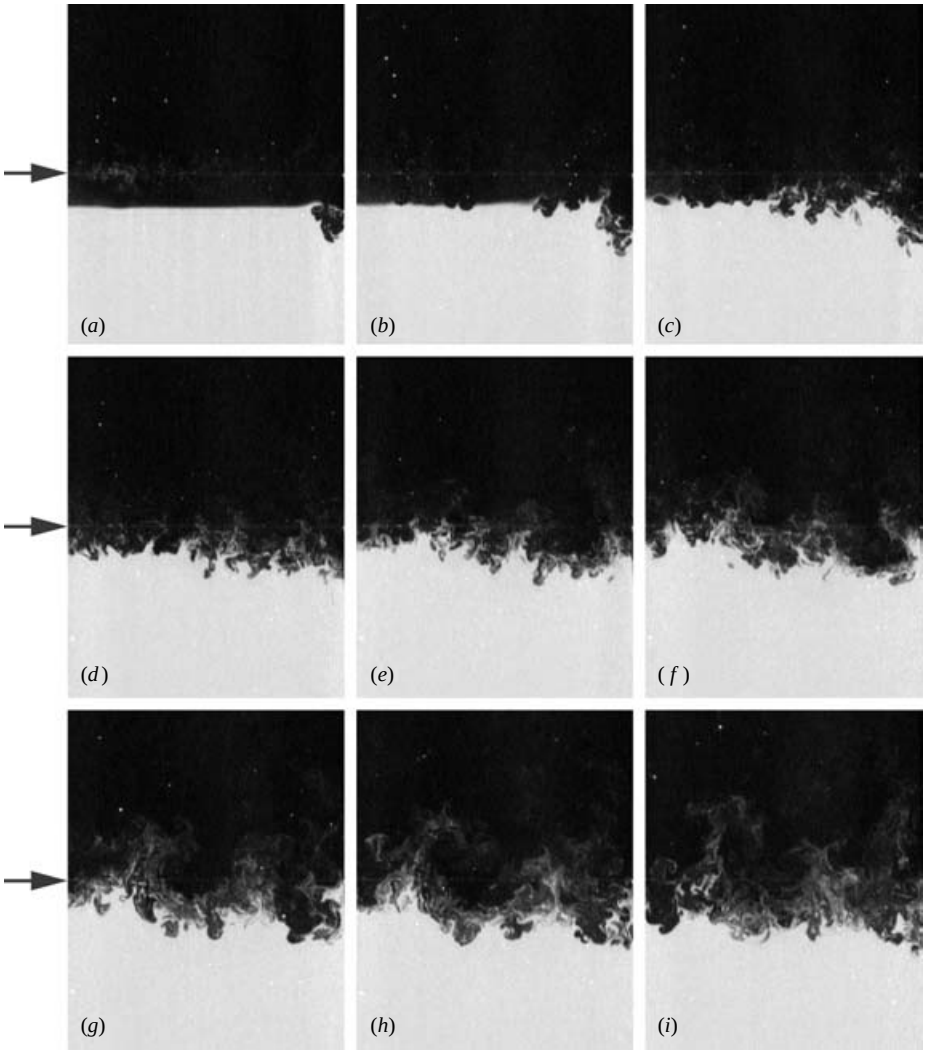

FIGURE 3. A sequence of LIF images for a typical $B = 0$ experiment with the fluorescent dye added to the bottom layer. Dimensionless times (τ_{12}) relative to the start of the barrier removal are: (*a*) 2.57, (*b*) 3.85, (*c*) 5.14, (*d*) 6.42, (*e*) 7.70, (*f*) 8.99, (*g*) 10.27, (*h*) 11.55, (*i*) 12.84. The arrows adjacent to the first column of images indicates the initial position of the upper interface ($h_2 = 5.0$ cm).

the sequence. However, it is clear that the volume of entrained fluid remains small when compared with the amount of fluid initially present in the bottom layer.

Figure 4 shows a sequence from an experiment where the density of the bottom layer is larger than that of the top layer ($\rho_3 > \rho_1$) In this case, the hydrostatic forces acting on the lower interface have been effectively doubled ($B = -1$ in this case, therefore $\rho_3 - \rho_2$ is twice as large as in the $B = 0$ experiments). Thus, although the instability that develops between the two upper layers is approximately the same as that of the $B = 0$ case, we can see that the deformation of, and entrainment across, the lower interface has been significantly decreased. As a result, very little of the bottom-layer fluid becomes mixed with either middle-layer or top-layer fluid.

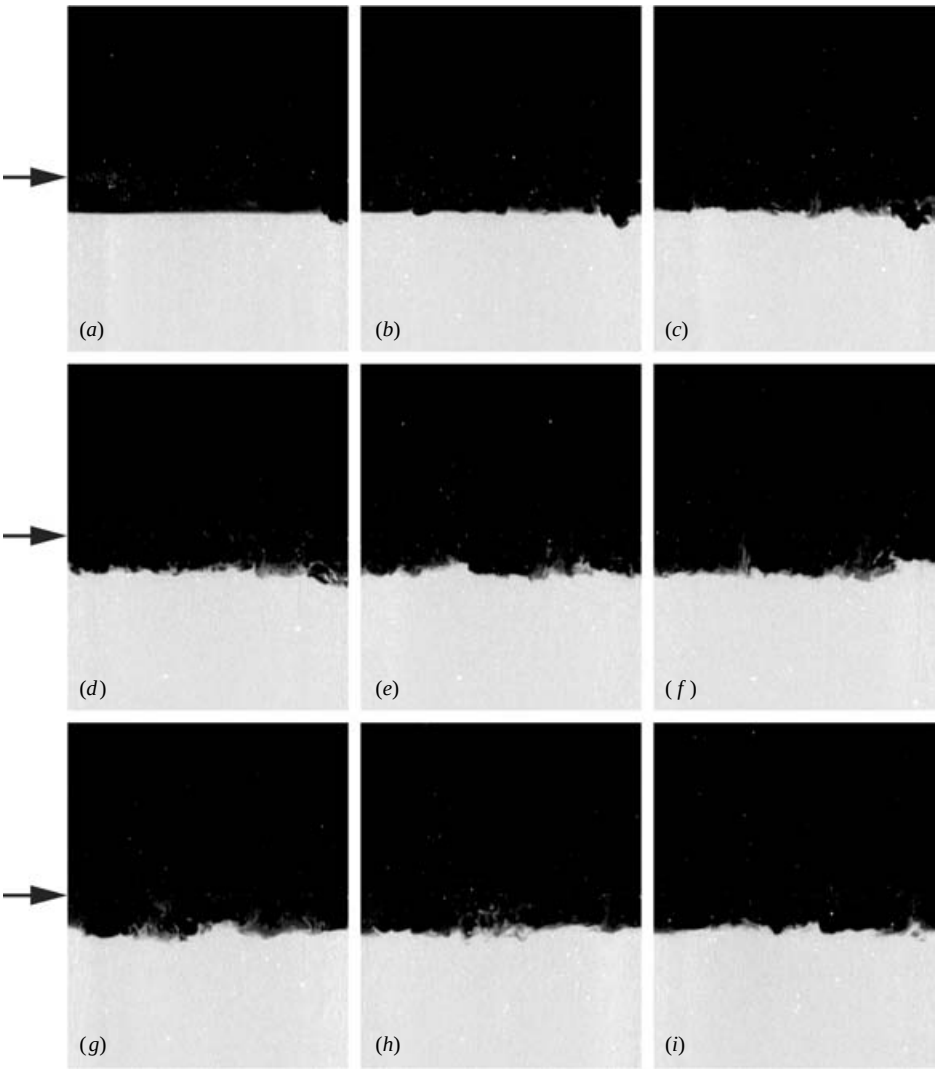

FIGURE 4. A sequence of LIF images for a $B = -1$ experiment. Dimensionless times (τ_{12}) relative to the start of the barrier removal are: (*a*) 2.57, (*b*) 3.85, (*c*) 5.14, (*d*) 6.42, (*e*) 7.70, (*f*) 8.99, (*g*) 10.27, (*h*) 11.55, (*i*) 12.84. The arrows adjacent to the first column of images indicates the initial position of the upper interface ($h_2 = 5.0$ cm).

Figures 5 and 6 show the effects of decreasing the density of the bottom layer so that it is less than that of the top layer ($\rho_3 < \rho_1$). In these experiments, hydrostatic forces acting across the lower interface are initially stabilizing, since ρ_3 is initially greater than ρ_2. However, as the instability of the upper interface develops, the density of the fluid immediately above the lower interface increases and eventually rises above that of the bottom layer. Thus, the lower interface eventually becomes Rayleigh–Taylor unstable. Figure 5 shows a $B = 0.25$ experiment, where deformation and entrainment of the lower layer is noticeably increased. Figure 6 shows a $B = 0.75$ experiment, where the Rayleigh–Taylor instability of the bottom layer progresses very quickly such that the entire bottom layer has been engulfed by the end of the sequence. Clearly, as A_{13}

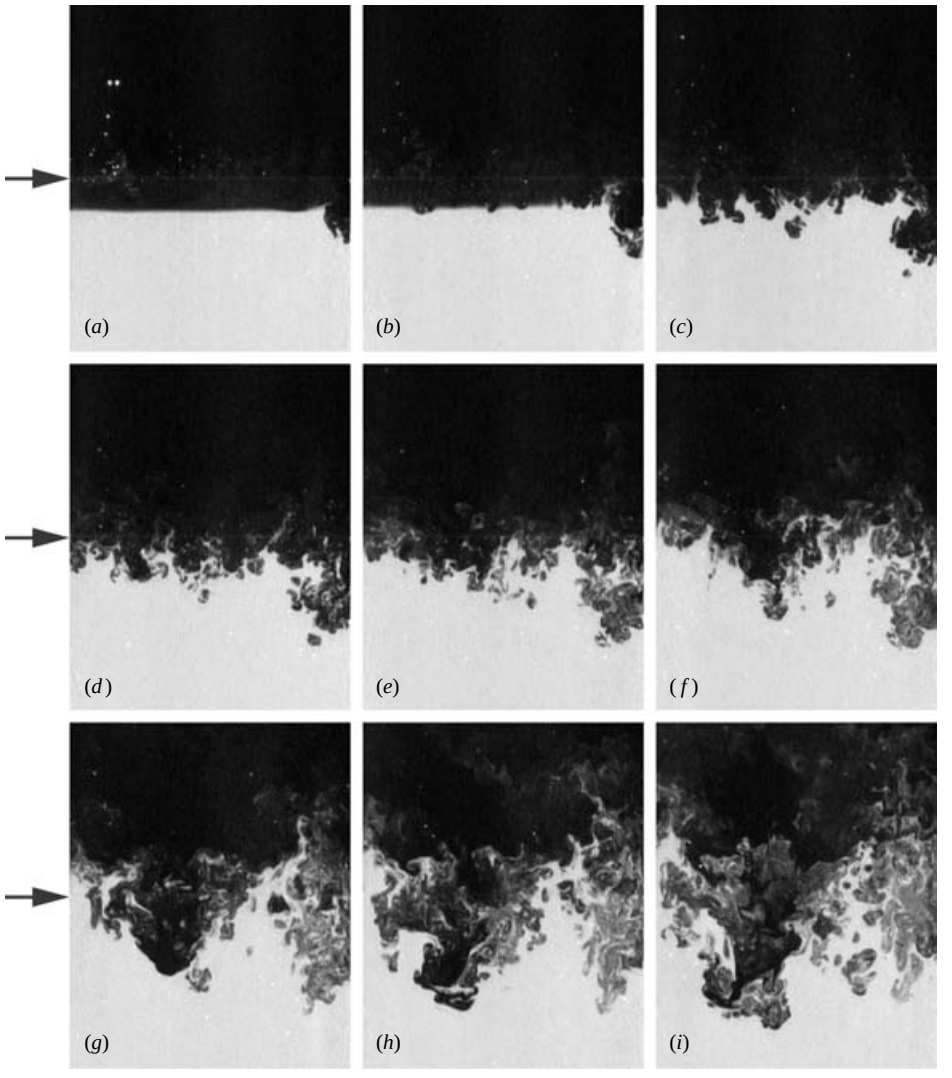

FIGURE 5. A sequence of LIF images for a $B = 0.25$ experiment. Dimensionless times (τ_{12}) relative to the start of the barrier removal are: (*a*) 2.57, (*b*) 3.85, (*c*) 5.14, (*d*) 6.42, (*e*) 7.70, (*f*) 8.99, (*g*) 10.27, (*h*) 11.55, (*i*) 12.84. The arrows adjacent to the first column of images indicates the initial position of the upper interface ($h_2 = 5.0$ cm).

approaches A_{12}, the stabilizing effect of the lower interface becomes negligible and the instability tends towards the classical two-layer case.

3.2. *Self-similarity*

One notable aspect of Rayleigh–Taylor instability is that, in its later stages of development, it has been found to exhibit properties of a self-similar turbulent flow (Read 1984; Linden *et al.* 1994; Snider & Andrews 1994; Dalziel *et al.* 1999; Dimonte & Schneider 2000). Self-similarity is attributed to the fact that in the later stages of development of the fully turbulent instability the perturbation spectrum is broadband and the higher-wavenumber aspects of the initial conditions are effectively 'forgotten'. Thus, there is no natural length scale other than that constructed by combining time

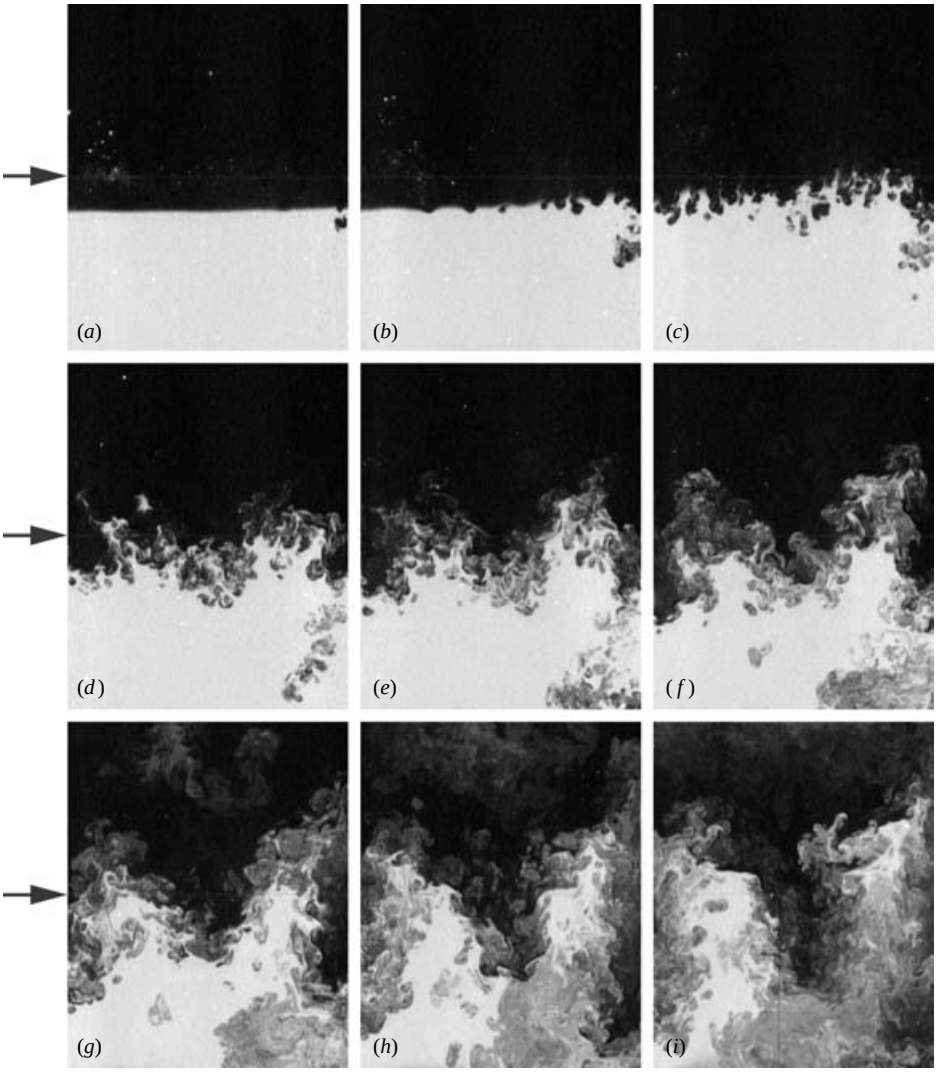

FIGURE 6. A sequence of LIF images for a $B = 0.75$ experiment. Dimensionless times (τ_{12}) relative to the start of the barrier removal are: (*a*) 2.57, (*b*) 3.85, (*c*) 5.14, (*d*) 6.42, (*e*) 7.70, (*f*) 8.99, (*g*) 10.27, (*h*) 11.55, (*i*) 12.84. The arrows adjacent to the first column of images indicate the initial position of the upper interface ($h_2 = 5.0$ cm).

with gravitational acceleration. Hence, the horizontally averaged distribution of any dependent variable (such as the density) presented in terms of the variable gt^2 should be independent of time (Youngs 1984). In the case of RT instability, the details of this distribution can most easily be determined by considering the conservation of energy of this flow. Note that the forgetting of the initial conditions is only an idealization, and that recent numerical studies suggest that initial conditions may affect the turbulent flow at late time (Cook & Dimotakis 2001). Nevertheless, self-similarity is a useful concept in that it provides expressions that have proved to be effective in describing the basic form of turbulent flows when allowed to evolve far from their initial states.

Single-interface analysis

Consider the Rayleigh–Taylor instability that develops on the interface between two semi-infinite incompressible fluids with densities ρ_1 and ρ_2. Let

$$\rho_0 = \begin{cases} \rho_1 & (z > 0), \\ \rho_2 & (z < 0), \end{cases}$$

designate the initial density distribution, then the conservation of mechanical energy (neglecting viscous dissipation) can be written:

$$g \int_{-\infty}^{\infty} \rho_0 z \, \mathrm{d}z = g \int_{-\infty}^{\infty} \overline{\overline{\rho}} z \, \mathrm{d}z + \tfrac{1}{2} \int_{-\infty}^{\infty} \overline{\overline{\rho q^2}} \, \mathrm{d}z, \tag{1}$$

where

$$\overline{\overline{(\cdot)}} = \operatorname*{Lim}_{X,Y\to\infty} \frac{1}{XY} \int_{-Y}^{Y} \int_{-X}^{X} (\cdot) \, \mathrm{d}x \, \mathrm{d}y,$$

and q is the magnitude of the velocity vector. Equation (1) states that the potential energy of the initially quiescent system must equal the sum of the potential and kinetic energies later on. Note that if the densities of the two fluids are nearly equal, then the Boussinesq approximation allows the density to be treated as a constant in the kinetic energy integral thus,

$$g \int_{-\infty}^{\infty} (\rho_0 - \overline{\overline{\rho}}) z \, \mathrm{d}z - \tfrac{1}{2} \rho \int_{-\infty}^{\infty} \overline{\overline{q^2}} \, \mathrm{d}z = 0. \tag{2}$$

Now, if the flow is assumed to be self-similar, then the distributions of density and kinetic energy can be formulated in terms of a similarity variable $\zeta = z/w(t)$ such that

$$(\rho_0 - \overline{\overline{\rho}}) = \hat{\rho}(t) f_\rho(\zeta),$$
$$\overline{\overline{q^2}} = \hat{q}^2(t) f_{q^2}(\zeta),$$

where w is the characteristic width of the mixed region. Therefore (2) becomes

$$g\hat{\rho} w \int_{-\infty}^{\infty} f_\rho(\zeta) \zeta \, \mathrm{d}\zeta - \tfrac{1}{2} \rho \hat{q}^2 \int_{-\infty}^{\infty} f_{q^2}(\zeta) \, \mathrm{d}\zeta = 0, \tag{3}$$

with significant contributions to the integrals only from $-1 < |\zeta| < 1$. Note that the integrals are independent of time. Furthermore, the magnitude of the kinetic energy should be proportional to the square of the growth rate of the mixed region. Thus, (3) yields

$$g\hat{\rho} w \propto \rho \left(\frac{\mathrm{d}w}{\mathrm{d}t} \right)^2.$$

In the case of Rayleigh–Taylor instability, the magnitude of the density perturbation is constant and proportional to the density difference, $\hat{\rho} \propto (\rho_1 - \rho_2)$, thus

$$w \propto Agt^2 \text{ as } A \to 0, \tag{4}$$

which is the well-known result. Note that the Atwood-number dependence in this result has previously been obtained using renormalization-group theory (Glimm, Zhang & Sharp 1991) and bubble-merger models (Alon *et al.* 1995).

Double interface analysis

In the two-interface RT problem investigated here, there are two regimes. At early times when $\tau_{12} \ll 1$, only the upper interface is unstable or active, thus the system

evolves as the two-layer system. However, at late times when $\tau_{12} \gg 1$, the lower interface plays a role. The similarity analysis described above for the single-interface system may also be applied to the late-time development of the two-interface system in the situation of a light fluid layer of height h_2 and density ρ_2 surrounded by fluid of density ρ_1. In this case

$$\rho_0 = \begin{cases} \rho_1 & (z > 0), \\ \rho_2 & (-h_2 < z < 0), \\ \rho_1 & (z < -h_2). \end{cases}$$

Since (2) remains unchanged, we may write.

$$g \int_{-\infty}^{\infty} (\rho_1 - \overline{\overline{\rho}}) z \, \mathrm{d}z - \tfrac{1}{2}(\rho_1 - \rho_2) g h_2^2 - \tfrac{1}{2}\rho \int_{-\infty}^{\infty} \overline{\overline{q^2}} \, \mathrm{d}z = 0. \tag{5}$$

Scaling density and kinetic energy distributions as above,

$$(\rho_1 - \overline{\overline{\rho}}) = \hat{\rho}(t) f_\rho(\zeta),$$
$$\overline{\overline{q^2}} = \hat{q}^2(t) f_{q^2}(\zeta),$$

but redefining the similarity variable ζ to allow for the fact that the density and kinetic energy distributions rise upward as the instability evolves,

$$\zeta = (z - z_0(t))/w(t),$$

results in

$$g\hat{\rho} w \int_{-\infty}^{\infty} f_\rho(\zeta) \left(\zeta + \frac{z_0}{w} \right) \mathrm{d}\zeta - \tfrac{1}{2}(\rho_1 - \rho_2) \frac{g {h_2}^2}{w} - \tfrac{1}{2}\rho \hat{q}^2 \int_{-\infty}^{\infty} f_{q^2}(\zeta) \, \mathrm{d}\zeta = 0.$$

However, in this case the scale of the density fluctuations $\hat{\rho}$ is not constant, but decreases with time. Nevertheless the behaviour of can be estimated by considering the conservation of mass:

$$\int_{-\infty}^{\infty} \rho_0 \, \mathrm{d}z = \int_{-\infty}^{\infty} \overline{\overline{\rho}} \, \mathrm{d}z. \tag{6}$$

Note that (6) can be rewritten as

$$\int_{-\infty}^{\infty} (\rho_1 - \rho_0) \, \mathrm{d}z = \int_{-\infty}^{\infty} (\rho_1 - \overline{\overline{\rho}}) \, \mathrm{d}z,$$

or

$$\hat{\rho} w \int_{-\infty}^{\infty} f_\rho(\zeta) \, \mathrm{d}\zeta = (\rho_1 - \rho_2) h_2, \tag{7}$$

making

$$\hat{\rho} w \propto (\rho_1 - \rho_2) h_2. \tag{8}$$

Using (7) to eliminate the second term in (5) yields,

$$g\hat{\rho} w \int_{-\infty}^{\infty} f_\rho(\zeta)(\zeta + z_0/w - h_2/2w) \, \mathrm{d}\zeta - \tfrac{1}{2}\rho \hat{q}^2 \int_{-\infty}^{\infty} f_{q^2}(\zeta) \, \mathrm{d}\zeta = 0.$$

For large times, where self-similarity is expected to apply, $w \gg h_2$, and we obtain

$$g\hat{\rho} w \int_{-\infty}^{\infty} f_\rho(\zeta)(\zeta + z_0/w) \, \mathrm{d}\zeta - \tfrac{1}{2}\rho \hat{q}^2 \int_{-\infty}^{\infty} f_{q^2}(\zeta) \, \mathrm{d}\zeta = 0,$$

which differs slightly from (3) by the inclusion of the z_0/w term in the first integral. However, if we restrict z_0/w to be constant, a reasonable assumption for self-similarity, then we again obtain

$$g\hat{\rho}w \propto \rho\left(\frac{\mathrm{d}w}{\mathrm{d}t}\right)^2.$$

Choosing $\hat{\rho} = (\rho_1 - \overline{\overline{\rho}})_{max}$, and $\int_{-\infty}^{\infty} f_\rho(\zeta)\,\mathrm{d}\zeta = 1$ defines

$$w = \frac{1}{(\rho_1 - \overline{\overline{\rho}})_{max}} \int_{-\infty}^{\infty} (\rho_1 - \overline{\overline{\rho}})\,\mathrm{d}z$$

and makes $\hat{\rho}w = (\rho_1 - \rho_2)h_2$. Thus,

$$(\rho_1 - \rho_2)gh_2 \propto \rho\left(\frac{\mathrm{d}w}{\mathrm{d}t}\right)^2$$

or

$$w = \gamma\sqrt{A_{12}gh_2}\,t \text{ as } A_{12} \to 0, \tag{9}$$

where γ is a (unknown) constant of proportionality. Therefore, at late time, the middle layer should grow linearly with time.

Now consider the conservation of a passive scalar C initially with unity concentration in the middle layer and zero elsewhere,

$$\int_{-\infty}^{\infty} \overline{\overline{C}}\,\mathrm{d}z = h_2. \tag{10}$$

Again, self-similarity requires

$$\overline{\overline{C}} = \hat{C}(t)f_C(\zeta),$$

so that (10) may be written as

$$\hat{C}w_C \int f(\zeta)\,\mathrm{d}\zeta = h_2.$$

Thus, $\hat{C} \propto (w_C/h_2)^{-1}$. Again, choosing $\hat{C} = C_{max}$ and $\int_{-\infty}^{\infty} f(\zeta)\,\mathrm{d}\zeta = 1$ defines

$$w_C = \frac{1}{C_{max}} \int_{-\infty}^{\infty} \overline{C}\,\mathrm{d}z,$$

thus,

$$\frac{1}{C_{max}} = \frac{w_C}{h_2} \propto \sqrt{\frac{A_{12}g}{h_2}}t. \tag{11}$$

Equation (11) provides the form of the spreading rate and the decrease in the maximum concentration of the self-similar mixing of a light fluid layer imbedded in a heavier medium. However, it should be stressed that this result does not dictate whether self-similarity will be achieved; that can only be determined by experimental measurement. The result above indicates only that if the flow is self-similar, the concentration of a passive scalar should follow the above relationship. It should also be mentioned that, in addition to spreading, the layer centre z_0 should rise slightly, owing to the effects of buoyancy. Furthermore, if self-similarity applies, this centre rises at a rate such that z_0/w is constant.

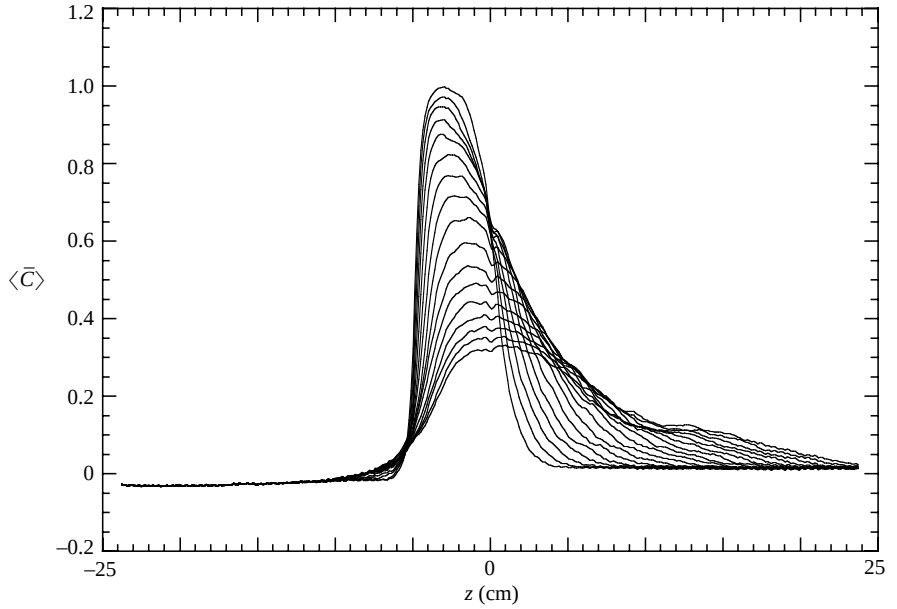

FIGURE 7. A plot of the ensemble-averaged mean concentration of twelve $B = 0$ experiments. Shown are profiles taken at dimensionless times in the interval $2.57 \leqslant \tau_{12} \leqslant 7.70$, separated by equal time increments of 0.385.

Experimental comparison

Figure 7 shows vertical profiles of $\langle \overline{C} \rangle$, the mean concentration found by taking the ensemble average of the horizontally averaged profiles of twelve $B = 0$ experiments in which the dye was originally mixed in the middle layer with $h_2 = 5.0\,\text{cm}$. Shown in this plot are profiles taken at dimensionless times in the interval $2.57 \leqslant \tau_{12} \leqslant 7.70$ separated by equal time intervals of 0.385. Thus, the transition from the initial distribution is not visible. Note that some dye is initially present in the top layer, resulting in slightly negative concentrations in the curves which have been adjusted to yield an average zero background level. This is a result of the fact that the middle layer must be slightly overfilled with dyed solution before the plate is inserted. Therefore, the excess becomes mixed with the undyed top-layer fluid. The curves of figure 7 show the steady decline of the maximum concentration C_{max} along with the spreading of the distribution. If this turbulent flow were self-similar, the shape of the curves in the later stages would be the same. Figure 8 shows 10 of these curves where the concentration has been scaled by C_{max}, and the vertical coordinate has been scaled and shifted using the width ($w_{1/2}$) and the centroid (z_{centre}) of that portion of the curve with $\langle \bar{C} \rangle$ greater than $C_{max}/2$. Choosing the centroid to align the curves is arbitrary, but more robust than using the z-location where C_{max} occurs. We can easily see that, except for an anomaly that begins to appear at $\tau_{12} = 5.78$ near the upper edge of the distribution, the curves fall on top of one another, demonstrating apparent self-similarity. (The anomaly is a result of three-dimensional boundary effects causing disturbances emanating from the front and back walls to intrude into the illuminated slice of the flow late in the experiments.)

Figure 9 provides an indication of the repeatability of the experiments by showing profiles of $\overline{C}$ at $\tau_{12} = 5.0$ for the 12 individual experiments making up the ensemble averages shown in figures 7 and 8. Note that this statistical variation shown graphically in this plot results in a 95% confidence interval for the ensemble mean values of

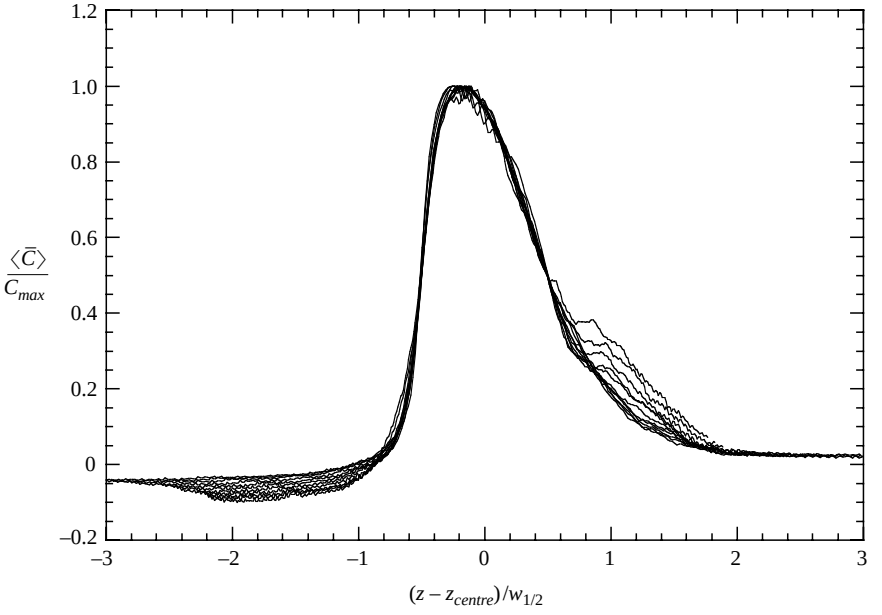

FIGURE 8. A plot of the scaled and shifted mean concentration curves of figure 7 illustrating self-similarity. Shown are profiles taken at dimensionless times in the interval $3.85 \leqslant \tau_{12} \leqslant 7.70$, separated by equal time increments of 0.385.

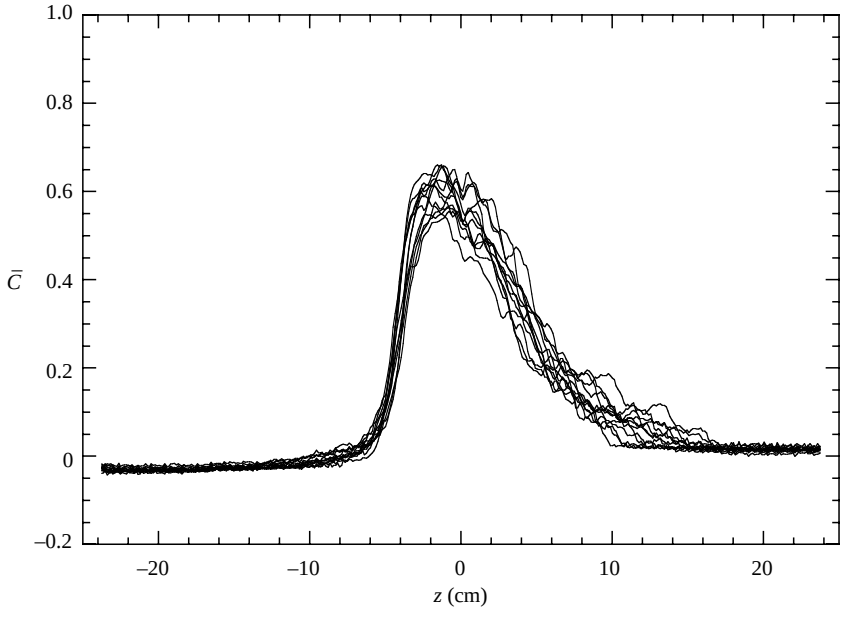

FIGURE 9. A plot of the individual mean concentration curves $\overline{C}$ at $\tau_{12} = 5.0$ for the 12 experiments making up the ensemble shown in figures 7 and 8.

approximately 0.03, and that this value is relatively constant in time in the later stages of these experiments. It should be mentioned that the finite barrier removal time slightly affects the mean profiles, producing additional variability as would

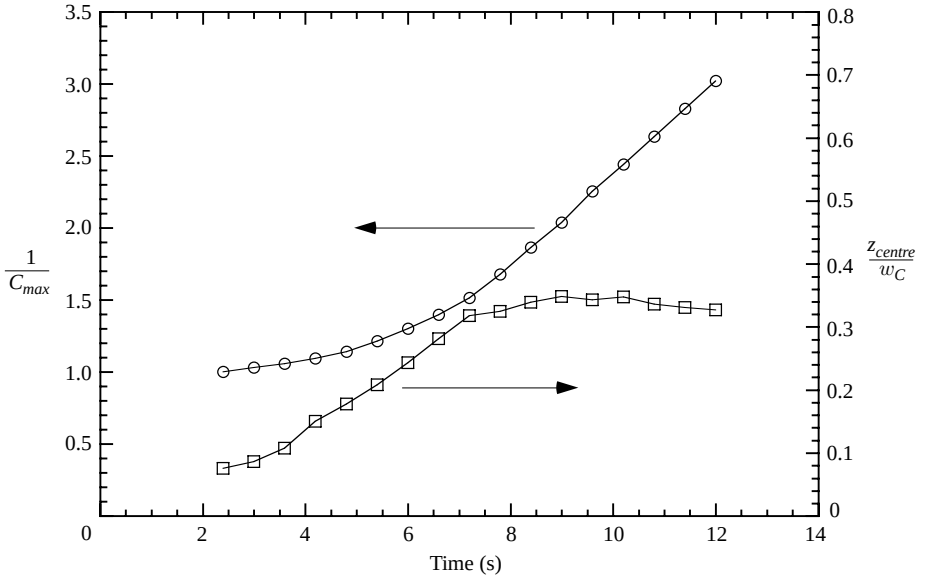

FIGURE 10. A plot of $1/C_{max}$ and z_{centre}/w_C for the $B = 0$ experiments with $h_2 = 5.0\,\text{cm}$.

be produced by averaging over fewer data. In addition, Dalziel (1994) compared statistics from measurements using a thin light sheet with those using a thick sheet thus producing averages over a greater depth in the viewing direction (60 mm) and found essentially no difference in the quantities discussed here.

If self-similarity is achieved, we would expect linear growth in the width of the central layer as given by w_C or $1/C_{max}$ late in the experiments, as indicated by (11). Note that we might also consider the width $w_{1/2}$, defined above, to be a suitable measure. However, of these three, $1/C_{max}$ can be measured with the greatest accuracy; thus, it is viewed as a more robust choice as a width measure. Figure 10 plots $1/C_{max}$ as a function of time for the experiments of figures 7 and 8 showing that indeed the curve appears to approach a straight line asymptotically late in the experiments. Also shown on this graph is a plot of $z_{centre}/w_C = z_{centre}C_{max}/h_2$, which should approach a constant value at late time, as appears to be the case. If the flow is self-similar, we would also expect the final growth rate of $1/C_{max}$ to depend upon the initial layer thickness in accordance with (11). Figure 11 plots $1/C_{max}$ as a function of the dimensionless time scale $\tau_{12} = (A_{12}g/h_2)^{1/2}t$ for the $B = 0$ experiments for three values of h_2. This plot shows that, indeed, the curves appear to asymptotically approach straight lines late in the experiments and that plotting against the dimensionless time scale clearly collapses the data at late time. Shown on this plot is the best-fit line to the data in the range $5 < \tau_{12} < 10$ which has a slope of 0.49 ± 0.03, where the error estimate is the 95% confidence interval found from the statistics of the curve fit. The convergence of the three curves in this plot strengthens the argument that self-similarity has been achieved. The agreement with (11) is further emphasized in figure 12 which plots the product of C_{max} and $\tau_{12} - \tau_0$ where τ_0 is a virtual time origin chosen to approximate the t-intercept of the late-time (linear) portion of the curves in figure 11. If self-similarity were achieved, we would expect the three curves in figure 12 to converge to a single horizontal line late in the experiments. The data show that this is indeed the case, indicating a constant of proportionality for (11) of approximately 0.5 (i.e. $w_C \approx 0.5\sqrt{A_{12}gh_2}\,t$).

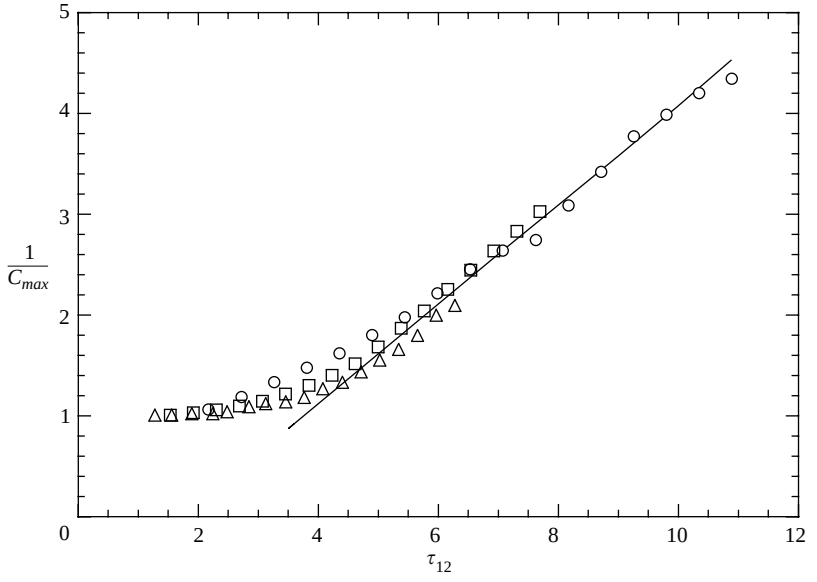

FIGURE 11. A plot of $1/C_{max}$ versus the dimensionless time scale τ_{12} for the three values of the middle-layer thickness. ○, $h_2 = 2.5\,\text{cm}$; □, 5.0 cm; △, 7.5 cm.

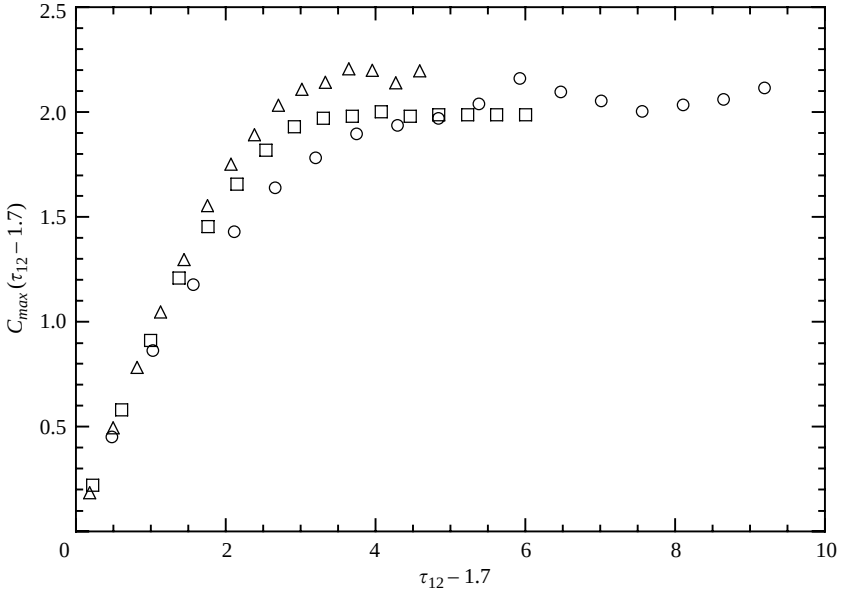

FIGURE 12. A plot of the product of C_{max} and $\tau_{12} - \tau_0$ where τ_0 is a virtual time origin chosen to approximate the x -intercept of the late-time (linear) portion of the curves in figure 11. Key as in figure 11.

Effect over overall stability

The self-similar relationship (11) developed in the section above strictly applies only to the case where $\rho_1 = \rho_3$ (i.e. $B = 0$). However, we should note that in the experiments where $\rho_1 \leqslant \rho_3$, the lower interface remains relatively flat at late times. It

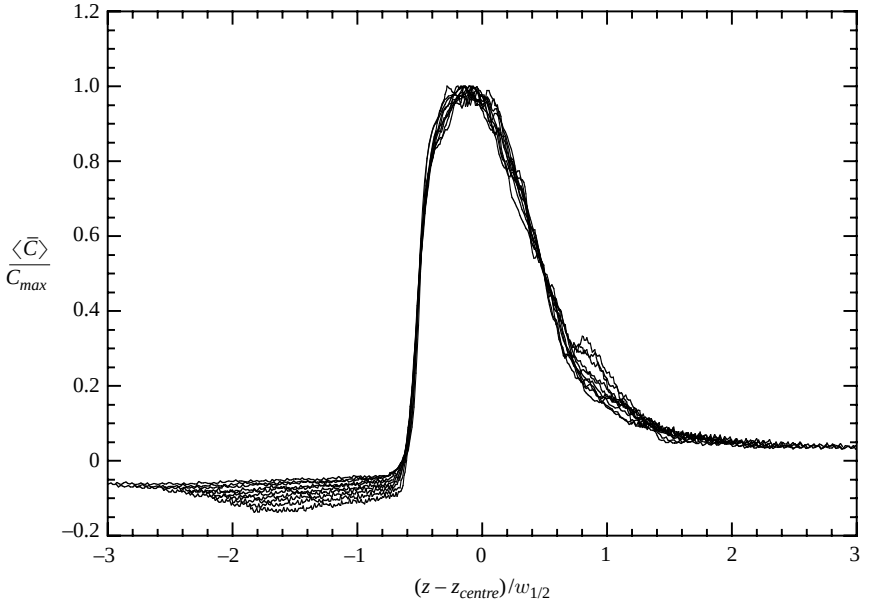

FIGURE 13. A plot of the scaled and shifted mean concentration curves of three $B = -1$ experiments illustrating self-similarity. Shown are profiles taken at dimensionless times in the interval $3.47 \leqslant \tau_{12} \leqslant 6.93$, separated by equal time increments of 0.385.

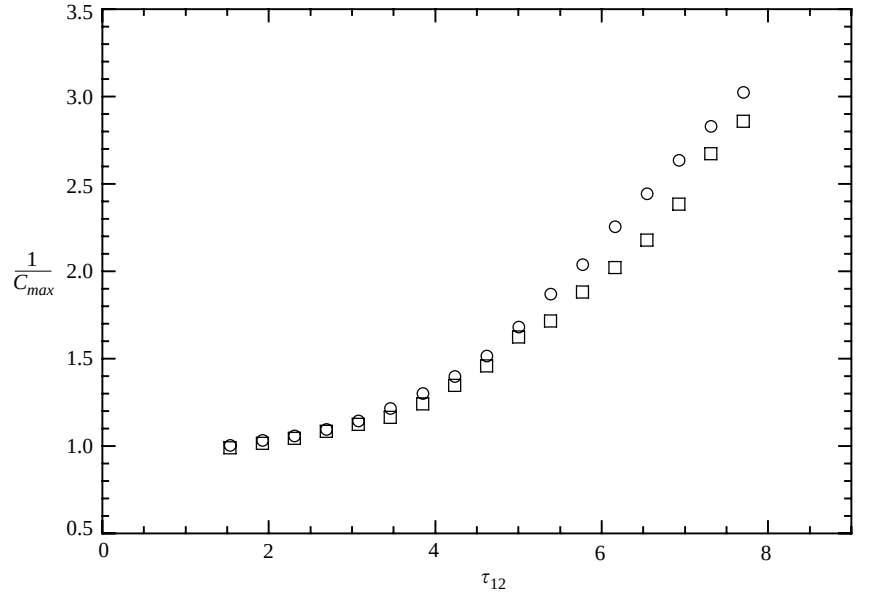

FIGURE 14. A plot of $1/C_{max}$ versus τ_{12} for ○, the $B = 0$ and □, $B = -1$ experiments.

therefore seems reasonable to model these experiments by considering the self-similar mixing of a light fluid layer bounded below by a solid wall. In this situation, the initial density distribution is

$$\rho_0 = \begin{cases} \rho_1 & (z > h_2), \\ \rho_2 & (0 < z < h_2), \end{cases}$$

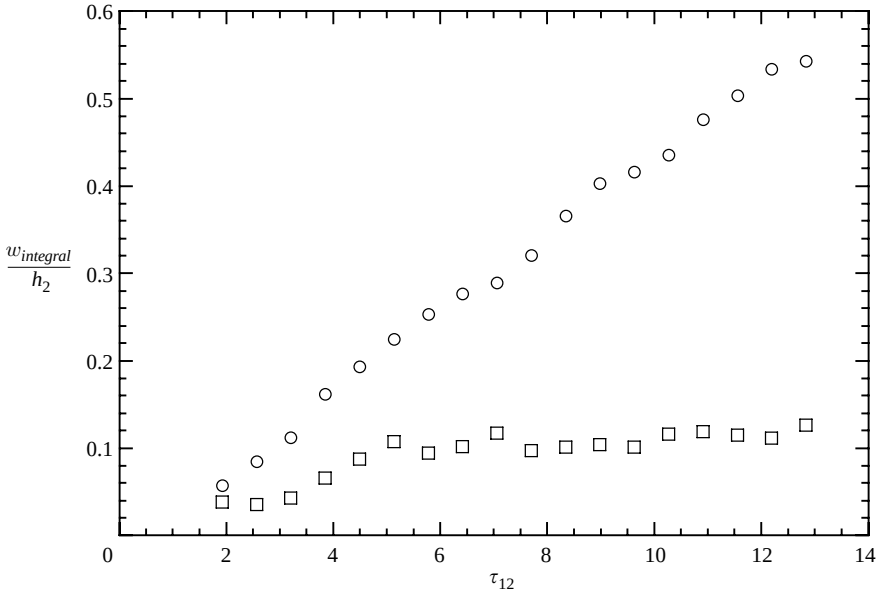

FIGURE 15. A plot of $w_{integral}/h_2$ for ○, the $B=0$ and □, $B=-1$ experiments.

and the only necessary modification to the analysis above would be to change the lower limits of the integrals from $z=-\infty$ to $z=0$. However, this change would yield a spreading rate identical to (11). Thus, we might also expect (11) to hold for all cases when $\rho_1 \leqslant \rho_3$. Figure 13 is a plot similar to figure 8, but for the $B=-1$ experiments. In this case, the ensemble average was taken over only three experiments. Nevertheless, the curves appear to collapse very well, suggesting self-similarity for this set of experiments. Figure 14 is a plot of $1/C_{max}$ versus τ_{12}, which compares the measurements from the $B=0$ and $B=-1$ experiments. The data show good agreement between the two sets of experiments, both showing linear growth at late time. The $B=-1$ experiments, however, do show a slight (7%) decrease in the rate of growth which can be attributed to the slower spreading of the lower stable interface.

It should be noted that the Reynolds number of these experiments is relatively small. In two-fluid Rayleigh–Taylor instability, the Reynolds number is usually defined using the vertical extent of the mixing zone and its spreading rate. For these experiments, if we choose the vertical extent of the spreading middle layer and its spreading rate, the Reynolds number defined this way achieves a value of approximately 2500 late in the experiments. This value, while being relatively low, is nevertheless comparable to the largest value achieved in current numerical simulations and is similar in size to earlier two-fluid experiments in the current apparatus, both of which have been shown to exhibit self-similar growth.

The slower spreading of the lower interface for the $B=-1$ experiments is further emphasized in figure 15 which shows a plot of,

$$w_{integral} = \int_{-H}^{H} \langle \overline{C} \rangle (1 - \langle \overline{C} \rangle)\, \mathrm{d}z,$$

which is a measure of the width of the lower interface, for different sets of the $B=0$ and $B=-1$ experiments in which the fluorescent dye has been placed in the bottom layer only. Note that self-similarity would dictate that this quantity would

also grow linearly with time, which appears to be verified by this plot for the $B = 0$ experiments. However, the larger density difference across the lower stable interface in the $B = -1$ experiments is shown to significantly slow its spreading rate, causing $w_{integral}$ to approach a small constant value, supporting the solid-wall assumption made above. Note that the data shown in this plot extend to significantly later time than those of figures 11 and 12, extending beyond the time that the upper boundary of the turbulent mixing zone reaches the top of the tank (at $\tau_{12} \approx 8$). It is therefore especially remarkable that $w_{integral}$ maintains its constant growth rate throughout this period.

The spreading rate of the middle-layer fluid in the $B = 0$ and $B = -1$ experiments is the result of mixing at two fronts: the upper RT unstable front driven by the gravitational instability of the light fluid layer, and the lower statically stable front acted upon by turbulence generated by the RT instability of the upper interface. Thus both these processes contribute to the observed self-similar spreading of the middle layer. However, since the lower interface in these experiments is stable and remains reasonably flat, its contribution to the mixing of the layer is small. Thus, the observed spreading of the layer shown in figures 11 and 14 is almost entirely the result of the development of the upper unstable mixing front, a result supported by the similarity of the mixing rates for the $B = 0$ and $B = -1$ configurations shown in figure 14. This makes it difficult to determine whether the self-similar behaviour observed in these experiments is the result of the self-similar spreading at both interfaces or simply the result of the self-similar spreading of the upper interface only, such as might be observed in the single-interface wall-bounded flow. Indeed the mixing at each front is produced by very different processes – RT instability at the upper front and ambient turbulence acting upon a stable interface at the lower front – suggesting that the self-similar behaviour of the type normally associated with RT instability is indicative of only the upper front. However, the constant growth rate of $w_{integral}$ for the $B = 0$ experiments observed in figure 15 indicates that the spreading of the lower interface is consistent with that of the upper. Thus, combined self-similarity might be applicable when $\rho_1 = \rho_3$.

3.3. *Erosion of the bottom layer*

The developing Rayleigh–Taylor instability of the upper unstable interface generates turbulence which then impacts and erodes the lower stable interface. Some insight into this process may be gained by considering the instability of the upper interface and its subsequent evolution separately from the processes controlling the lower interface. If the instability of the upper interface proceeds without mixing, then fluid of density ρ_1 is brought in contact with the bottom layer. Ignoring the kinetic energy this fluid may contain, the lower interface will be unstable if $\rho_1 > \rho_3$ corresponding to $B > 0$, or stable if $\rho_1 < \rho_3$ ($B < 0$). However, mixing between the upper and middle layers releases less potential energy and also reduces the density that the lower layer is exposed to, allowing the possibility of global stability even when $B > 0$. To determine whether a configuration is ultimately stable or unstable, we must consider the limiting case in which the top and middle layers are fully mixed at late times. The high mixing efficiencies reported by previous authors (e.g. Linden *et al.* 1994; Holford *et al.* 2003) suggest that this should be a reasonable approximation. In this situation, the post mixing density just above the lower interface is $\rho_{mix} = (h_1\rho_1 + h_2\rho_2)/(h_1 + h_2)$, giving an effective Atwood number for the lower interface of

$$A_{mix} = A_{13} - \frac{h_2}{h_1 + h_2} A_{12}.$$

Thus, $A_{mix} > 0$ indicates static stability.

This static stability condition, of course, is only part of the story. The flow will have significant kinetic energy by the time it reaches the lower interface. The presence of kinetic energy suggests that even if the flow is stable according to the above criteria, it may penetrate into or erode away the lower layer. In such a case, the controlling parameter for this penetration or erosion process will be a Richardson number,

$$Ri = \frac{\Delta\rho g \ell}{\rho u^2},$$

where ℓ and u are characteristic turbulent length and velocity scales, respectively. Self-similarity will ensure that these will scale with the width and growth rate of the mixing layer. Using the standard single-interface RT growth $\ell \sim w = \alpha A_{12} g t^2$ and $u \approx \beta A_{12} g t = \beta (A_{12} g h/\alpha)^{1/2}$ for the instability of the upper interface and assuming a linear density distribution $\rho(z) = (\rho_1 + \rho_2)/2 - (\rho_1 + \rho_2) z/(2h)$ yields the Richardson number at the moment when the mixed region first contacts the lower layer

$$Ri = \frac{2\alpha}{\beta}\left(1 - \frac{A_{13}}{A_{12}}\right),$$

that does not depend on the depth of the layers. This parameterization, however, is insufficient by itself to describe the flow fully.

The study of mixing across stably stratified interfaces is often studied in the laboratory by considering mixing induced by oscillating a grid a distance above or below a stable density interface (Fernando 1991). In these experiments the entrainment rate, defined as $E = u_e/u$, where u_e is the entrainment velocity, has been found to have a power law dependence on the Richardson number, i.e.

$$E \propto Ri^{-n}, \tag{12}$$

for $Ri \gtrsim 1$. The value of the exponent n is typically measured in these studies; however, its value has been observed to vary over a fairly wide range (from 1 to 1.75) and to be a function of the Schmidt number. The oscillating grid experiments resemble the state of our system at late time in the $B = 0$ and $B = -1$ experiments (except that the turbulence driving the entrainment is the result of RT instability rather than mechanical stirring) suggesting that (12) may also apply here. To explore this possibility, we begin by rewriting the Richardson number in terms of our similarity solution. In particular, noting that the similarity solution inherently requires the turbulent length scales to scale with the width w, and the turbulent fluctuations to scale with the growth rate $\mathrm{d}w/\mathrm{d}t$, we define an instability-driven Richardson number appropriate for the $B = 0$ experiments

$$Ri_{RT} = \frac{\hat{\rho} g w}{\rho(\mathrm{d}w/\mathrm{d}t)^2}.$$

However, using (8) and since the linearity of (9) implies $\mathrm{d}w/\mathrm{d}t$ is constant, we find

$$Ri_{RT} = \frac{2}{\gamma^2},$$

which is independent of time. In particular, for the $B = 0$ experiments described earlier, we find $\gamma \approx 0.5$ and $Ri \approx 8$.

The situation will change and our similarity model will no longer be valid once the upper edge of the mixing zone reaches the top of the container. Simulations (e.g. Youngs 1991) and experiments (e.g. Dalziel 1993) have demonstrated that for classical Rayleigh–Taylor instability, the total kinetic energy begins to decrease from the time

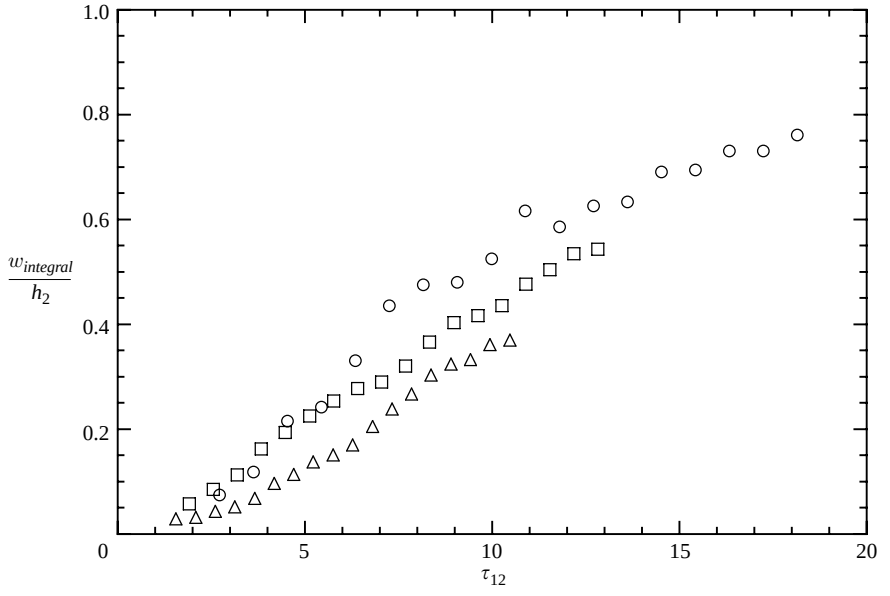

FIGURE 16. A plot of $w_{integral}/h_2$ for the three values of the middle-layer thickness. ○, $h_2 = 2.5$ cm; □, 5.0 cm; △, 7.5 cm.

the instability reaches the boundary. While we expect a similar situation to occur here, we note that it will take some time for the halting of further growth of the instability to be communicated back to the lower interface. Indeed, we would expect this to scale with the turnover time $w/(\mathrm{d}w/\mathrm{d}t)$ at the time when the mixing zone reaches the top. From (9), we see that this time scale is simply the time it takes for the mixing zone to reach the top, and so we anticipate the Richardson number will remain approximately constant for a long time after the growth of the instability has ceased.

Returning to (12) and noting again that $u \propto \mathrm{d}w/\mathrm{d}t$, we can now relate the entrainment velocity to the results of our similarity model,

$$u_e \propto \frac{\mathrm{d}w}{\mathrm{d}t} Ri_{RT}{}^{-n} = \gamma \sqrt{A_{12} g h_2} \left(\frac{2}{\gamma^2}\right)^{-n}, \tag{13}$$

which is constant during the active phase of the RT instability. In our experiments, u_e can be interpreted as the growth of the region containing bottom-layer fluid. This growth is characterized by $\mathrm{d}w_{integral}/\mathrm{d}t$. Integrating (13) suggests that

$$w_{Integral} \propto w Ri_{RT}{}^{-n} \propto h_2 \tau_{12}. \tag{14}$$

The experimental agreement with (14) is illustrated in figure 16 which plots $w_{integral}/h_2$ versus τ_{12} for the $B = 0$ experiments. In this case, the Richardson number is the same for the three sets of experiments having different values of h_2. Therefore the three curves should have the same slope at late time, which appears to be verified by the data. That (14) is linear in time provides additional support for our similarity model. Indeed, our very assertion of self-similarity means that since we found w to be linear in time, then $w_{integral}$ must also be linear or else the model is invalid. It is important to note, however, that the linearity of $w_{integral}$ is not a direct consequence of the linearity of w, but rather a consequence of the Richardson-number-dependent entrainment law

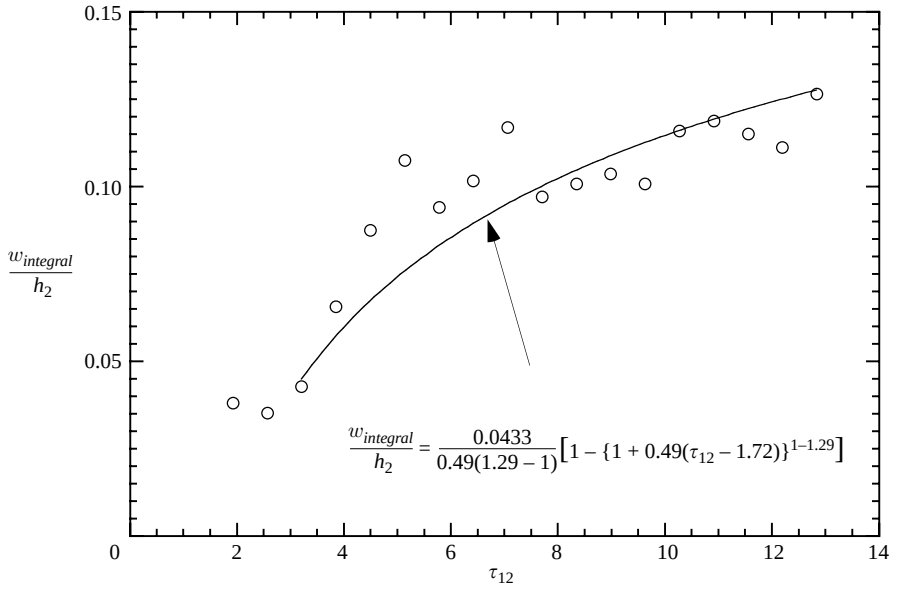

FIGURE 17. A plot of $w_{integral}/h_2$ for the $B=-1$ data of figure 15 along with a curve fit of a function of the form (16) yielding the Richardson number exponent of $n=1.29$.

we have used. This consistency between separately and independently derived models is reassuring, but ultimately is a necessary consequence of dimensional analysis.

The Richardson number can be modified slightly to describe the situation of a bottom-layer density ρ_3 differing from ρ_1 if we assume that the turbulent flow generated by development of the instability of the middle layer is the same as that in the $B=0$ configurations. This assumption is reasonable as experiments with grid-generated turbulence in a variety of configurations suggest that only around 5% of the available kinetic energy is lost to mixing across an interface at these Richardson numbers (Holford & Linden 1999). Defining $\Delta\rho = (\rho_3 - \overline{\overline{\rho}})_{max} = \hat{\rho} - (\rho_1 - \rho_3)$, we find

$$Ri_{RT} = \frac{2}{\gamma^2}\left[1-\gamma\frac{A_{13}}{A_{12}}\sqrt{\frac{A_{12}g}{h_2}}t\right] = \frac{2}{\gamma^2}(1-\gamma B\tau_{12}).$$

Thus, the Richardson number in the $B=-1$ experiments is time dependent. Rewriting (13) in terms of the time-dependent Richardson number yields

$$\frac{\mathrm{d}}{\mathrm{d}\tau_{12}}\left(\frac{w_{integral}}{h_2}\right) \propto \frac{\mathrm{d}}{\mathrm{d}\tau_{12}}\left(\frac{w}{h_2}\right) {Ri_{RT}}^{-n} = \gamma\left[\frac{2}{\gamma^2}(1-\gamma B\tau_{12})\right]^{-n},$$

which can be integrated to obtain

$$\frac{w_{integral}}{h_2} \propto -\frac{1}{B(n-1)}\left(\frac{2}{\gamma^2}\right)^{-n}[1-(1-\gamma B\tau_{12})^{1-n}] \quad \text{for } n\neq 1. \tag{15}$$

Thus, it would appear reasonable to curve fit a function of this form to the $B=-1$ case of figure 15 to extract a value for the exponent n (figure 17). Unfortunately, the amount of scatter and lack of curvature of this data do not yield reliable values for both a proportionality constant and exponent n. However, if we assume that the constant of proportionality in (15) is the same for both $B=0$ and $B=-1$, this constant can be reliably extracted from the $B=0$ data of figure 15 by fitting a line

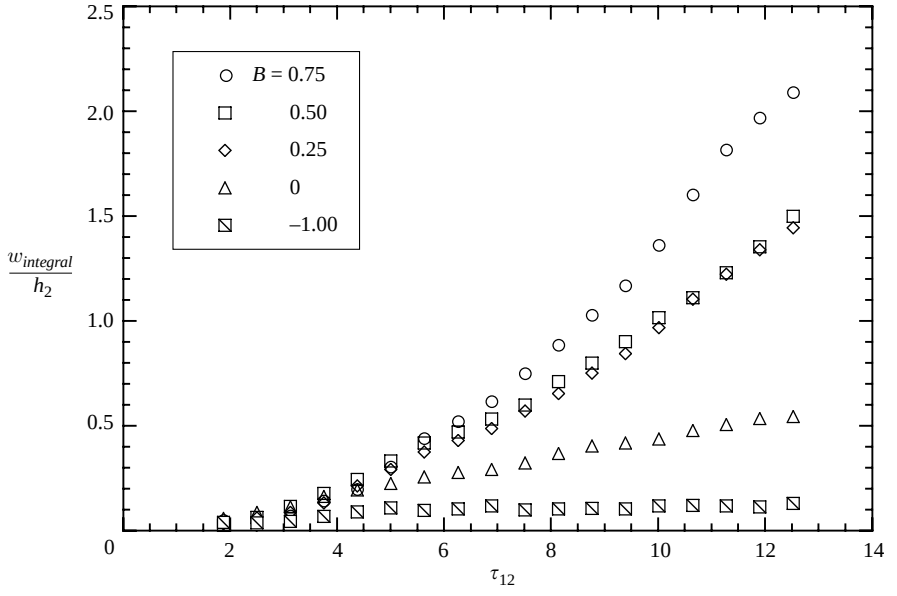

FIGURE 18. A plot of $w_{integral}/h_2$ for experiments where B is varied from -1 to 0.75.

to the data which yields a slope 0.0433 ± 0.002. Then fitting a function of the form

$$\frac{w_{integral}}{h_2} = \frac{0.0433}{0.49(n-1)}[1 - \{1 + 0.49(\tau_{12} - 1.72)\}^{1-n}] \tag{16}$$

(which uses the virtual time origin found in the section above) to the $B = -1$ data yields a value of $n = 1.29$, which lies in the middle of the range found in oscillating grid experiments. The 95% confidence interval based on the errors of the components used to compute this value is $\pm$ 0.14. However, the accuracy of this computed exponent is probably more strongly influenced on assumptions made in deriving (16).

While, for the present experiments, we do not have any direct measurements of the mixing efficiency for the lower interface, we anticipate that the mixing efficiency would be comparable with that found for mixing-box experiments owing to the similarity in the entrainment mechanism and exponent for the entrainment law. This efficiency, typically around 5% in mixing-box experiments, is substantially lower than the nearly 50% efficiency found in two-layer Rayleigh–Taylor instability. Thus, as we suggested earlier, the energy lost to mixing across the lower interface from the developing instability is minimal.

3.4. *The late-time unstable configuration*

Figure 18 shows $w_{integral}$ for all of the experiments including those where at late time, the lower interface is Rayleigh–Taylor unstable (i.e. $B > 0$). In contrast to the cases with stable late-time stratifications ($B = -1$ and 0), which appear to grow linearly with time, the $B > 0$ cases clearly show the accelerating growth behaviour of two-layer Rayleigh–Taylor instability. Figure 19 replots the $B > 0$ data as $w_{integral}/h_3\tau_{13}^2 = w_{integral}/A_{13}gt^2$, where $\tau_{13} = (A_{13}g/h_3)^{1/2}t$. That the two most unstable configurations ($B = 0.5$ and 0.75) converge to a constant of approximately 0.02 (i.e. $w_{integral} \rightarrow 0.02A_{13}gt^2$) indicates self-similar behaviour similar to that found in two-layer Rayleigh–Taylor instability. Indeed, this value is in close agreement with the value

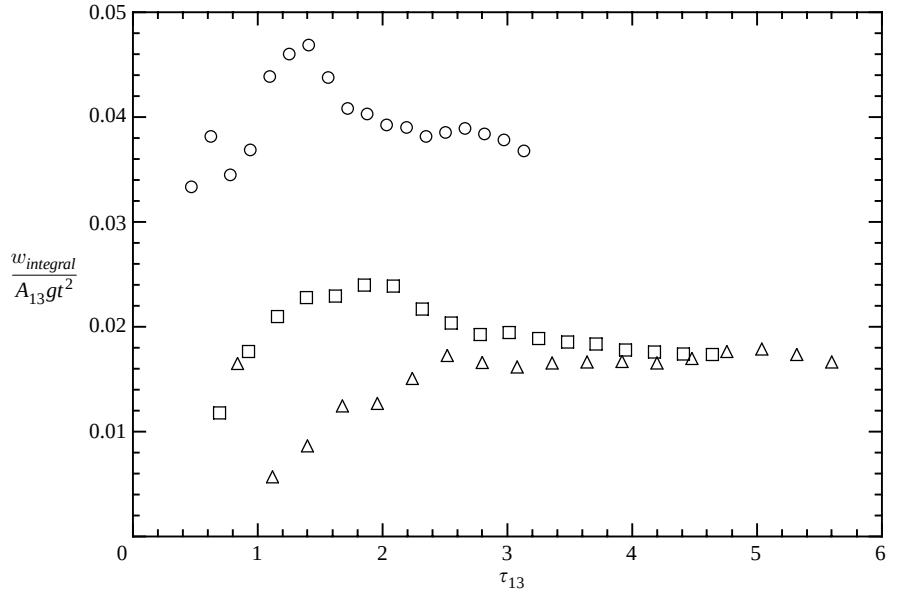

FIGURE 19. A plot of $w_{integral}/A_{13}gt^2$ which should cause the unstable configurations to converge to a single horizontal line late in the experiments if they follow Rayleigh–Taylor self-similarity. ○, $B = 0.25$; □, 0.50; △, 7.5.

obtained from the earlier single-interface Rayleigh–Taylor experiments of Dalziel *et al.* (1999) which found this constant to be approximately 0.023. Also, if we assume a linear mean concentration profile, which would make $w_{integral} = \delta/3$ where δ is the half-layer width, our result yields a value of α in good agreement with the experiments of Dimonte & Schneider (2000). Thus, in the case of the two most unstable configurations, the presence of the middle layer is relatively unimportant. The turbulence generated by the instability of the upper interface (which is driven by the stronger A_{12} density contrast), and the dilution effect of the presence of the middle layer (which reduces the density contrast across the lower interface), appears to produce very little effect on the growth of the instability of the lower interface, although we expect that if the depth of the middle layer were sufficiently large, then the dilution of the top-layer fluid before it reached the bottom layer would play a role. The least unstable configuration ($B = 0.25$) similarly converges to a horizontal line in figure 19. However, in this case, the constant of proportionality is approximately twice as large. Thus, in this case, the turbulence generated by the instability of the upper interface has a much more pronounced effect on the slower-growing late-time instability. The background turbulence generated by the instability of the upper interface, which is much stronger than that produced by the instability between the top- and bottom-layer fluids, apparently produces a significant increase in the mixing rate across the lower interface.

3.5. *Molecular mixing*

The integral measure of interface width, $w_{integral}$, includes the effects of both molecular mixing and surface deformation in that both diffusion and surface deformation will result in an increase in this parameter. In order to investigate the relative importance

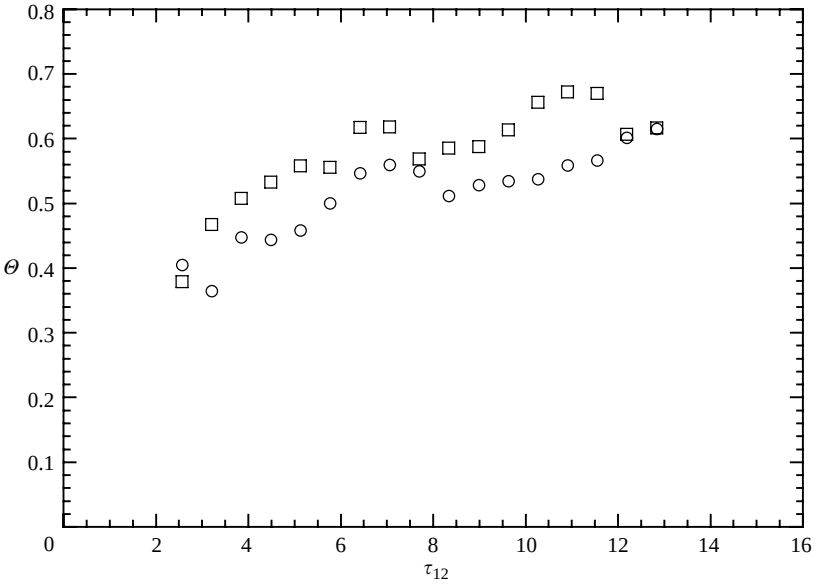

FIGURE 20. A plot of the global mixing fraction for the late-time stable configurations. ○, $B = 0$; □, -1.

of these two processes, Linden *et al.* (1994) defined the global mixing fraction

$$\hat{\Theta} = \int_{-H}^{H} \overline{\langle C(1-C)\rangle}\,\mathrm{d}z \Big/ \int_{-H}^{H} \langle\overline{C}\rangle(1-\langle\overline{C}\rangle)\,\mathrm{d}z, \tag{17}$$

which is a measure of the fraction of $w_{integral}$ that can be attributed to molecular mixing alone. Note that the numerator of (17) is an integral measure similar to $w_{integral}$. This is proportional to the quantity of mixed fluid and is insensitive to the effects of surface deformation. Thus, $\hat{\Theta} = 0$ when there is no molecular mixing and $\hat{\Theta} \to 1$ when the system becomes uniformly mixed. It should be stressed that the resolution of the images and the thickness of the light sheet are not adequate to resolve the Kolmogorov scale, estimated as $\eta \sim \delta Re_\delta^{-3/4}$ where Re_δ is a suitably chosen Reynolds number. In these experiments, the Reynolds number, defined using the vertical extent of the spreading middle layer and its spreading rate, achieves a value of approximately 2500 late in the experiments thus yielding a value of $\eta \approx 0.4$ mm. Note that the diffusion scale is much smaller than the Kolmogorov scale owing to the relatively large value of the Schmidt numbers for both salt (≈ 200) and fluorescein (≈ 2000). Therefore, the image data are incapable of capturing the finest scalar fluctuations. However, since $\hat{\Theta}$ has been calculated in the previous RT experiments which had similar resolution limitations, it is useful to compute $\hat{\Theta}$ for our experiments in order to make comparison with the previous two-layer experiments.

Figure 20 is a plot of $\hat{\Theta}$ for the late-time stable configurations with $B = 0$ and $B = -1$. In this plot, the mixing fraction is observed to be relatively constant, attaining a value of 0.5 to 0.6 at late time. This time independence is anticipated since we should expect $\hat{\Theta}$ to be constant in a self-similar flow. Figure 21 is a similar plot for the late-time Rayleigh–Taylor unstable configurations ($B > 0$). Note that in this case, $\hat{\Theta}$ appears to approach 0.8 at late times, a result in agreement with the two-layer RT experiments of Linden *et al.* (1994). However, the convergence toward this value does not occur until very late time, at which point the finite volume of the fluid container

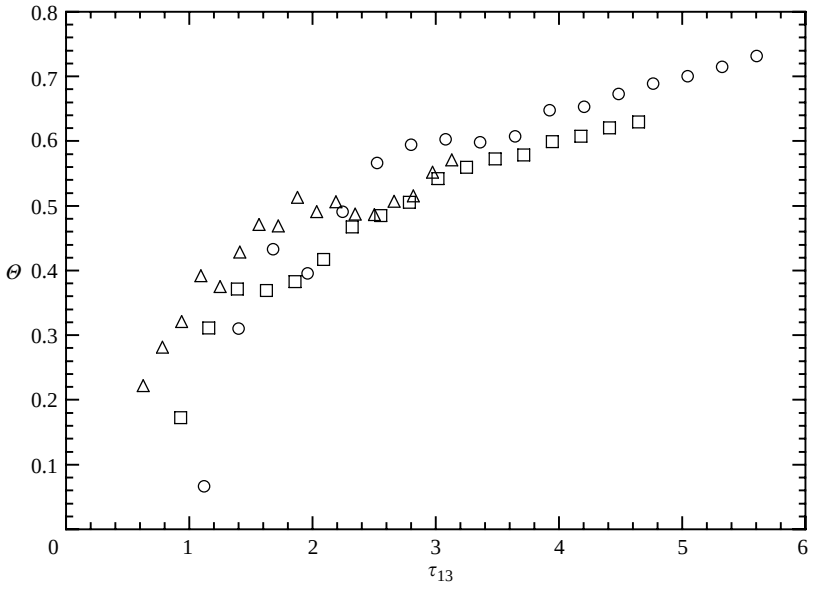

FIGURE 21. A plot of the global mixing fraction for the late-time unstable configurations. ○, $B = 0.75$; □, 0.50; △, 0.25.

is an important influence. We anticipate that if the instability were allowed to evolve in an infinite container, and thus remained self-similar, we should expect a constant value of $\hat{\Theta}$, similar to the late-time stable RT experiments of figure 20. This indeed appears to occur at intermediate times in figure 21 where we can see a levelling off in the value of $\hat{\Theta}$ again at a value of approximately 0.5 to 0.6. However, self-similarity will be broken at late time, when the mixing zone reaches the container top, spurring the further increase in $\hat{\Theta}$, driving it towards its asymptotic value.

4. Conclusions

The experiments presented here study the Rayleigh–Taylor instability of a three-layer system having one unstable and one stable interface. Most of the experiments were conducted with the density of the fluid in the bottom layer equalling that in the top layer. In this case, measurements of the horizontally averaged concentration of a fluorescent dye mixed in the middle layer suggests that the instability grows self-similarly in time, as demonstrated by the collapse of the mean concentration profiles when plotted in similarity coordinates. Self-similarity is further indicated because the width of the mean profiles is found to grow linearly in time, which is consistent with a buoyancy-driven self-similar flow that conserves both mass and mechanical energy. Collapse of the mean concentration profiles and linear growth of the width is also observed when the density of the bottom layer is increased above that of the top layer. However, because the mixing rate in these experiments is dominated by the Rayleigh–Taylor mixing occurring at the upper front, the observed self-similarity may only be indicative of the spreading of the upper interface such as would occur in the RT instability of a light fluid layer bounded below by a solid wall.

In the configuration where the top- and bottom-layer densities are the same, the erosion of the bottom-layer fluid by the turbulence generated by the upper unstable interface is found to be small owing to the fact that this interface is always stably

stratified. When the density of the bottom layer is increased above that of the top layer, the degree of erosion is further decreased. In the cases where the lower interface is stably stratified at late time, the spreading rate of the interface is found to be in agreement with an entrainment assumption in the form of a power law of the Richardson number with an exponent of approximately 1.3. This result is in good agreement with studies of the mixing across a stably stratified interface by turbulence generated using oscillating grids, and we anticipate that other related quantities, such as the mixing efficiency of this entrainment, will also be similar. Introduction of the entrainment hypothesis acts as a closure to our similarity model, and yields a constant rate of erosion of the bottom layer as the top of the mixing zone advances towards the top of the container. Although the similarity model breaks down once the mixing zone reaches the top, the entrainment across the lower interface continues to be constant for the eddy turnover time required to communicate this back to the lower interface.

When the density of the bottom layer is decreased below that of the top layer, the erosion increases as expected. However, in this case, the overall density distribution is such that it is Rayleigh–Taylor unstable at late time (i.e. $\rho_1 > \rho_3$ and $h_2 \ll h_1$,). In this situation, the turbulent mixing region at late times is found to grow similarly to that of single-interface Rayleigh–Taylor instability that lacks the middle layer with approximately the same value of the growth constant. In these experiments, the global mixing fraction approaches 0.8, in agreement with the earlier two-layer study of Linden *et al.* (1994). However, at intermediate times in the development, where we would expect self-similarity, the mixing fraction appears to take on a constant value.

The central role of Rayleigh–Taylor instability in mixing in geophysical and industrial flows is widely recognized. While our understanding of the dynamics of the instability, and the role played by the initial conditions, has increased greatly in recent years, most previous work has been restricted to the 'ideal' situation of a nominally planar horizontal interface separating two layers of approximately equal depth. However, naturally occurring manifestations of the instability will seldom arise from such ideal conditions. In geophysical flows, the instability will often develop as the result of breaking internal gravity waves, giving initial conditions characterized by both shear and complex stratifications that contain both stable and unstable portions. While the present study does not address directly the issue of the mixing produced, it does offer insight into the way that the turbulence generated by the instability can drive an entrainment across a neighbouring stable interface. Of key importance here is that the entrainment law appears to be consistent with that found from other sources of external mixing experiments.

REFERENCES

Alon, U., Hecht, J., Ofer, D. & Shvarts, D. 1995 Power laws and similarity of Rayleigh–Taylor and Richtmyer–Meshkov mixing fronts at all density ratios. *Phys. Rev. Lett.* **74**, 534–537.

Baines, W. D. 1975 Entrainment by a plume or jet at a density interface. *J. Fluid Mech.* **68**, 309–320.

Balmforth, N. J., Llewellyn Smith, S. G. & Young, W. R. 1998 Dynamics of interfaces in a stratified turbulent flow. *J. Fluid Mech.* **355**, 329–358.

Briggs, D. A., Ferziger, J. H., Koseff, J. R. & Monismith, S. G. 1998 Turbulent mixing in a shear-free stably stratified two-layer fluid. *J. Fluid Mech.* **354**, 175–208.

Cook, A. W. & Dimotakis, P. E. 2001 Transition stages of Rayleigh–Taylor instability between miscible fluids. *J. Fluid Mech.* **443**, 69–99.

Dalziel, S. B. 1993 Rayleigh–Taylor instability: experiments with image analysis. *Dyn. Atmos. Oceans* **20**, 127–153.

Dalziel, S. B. 1994 Final report: molecular mixing in Rayleigh–Taylor instability. Report for AWE, 91 pp.

Dalziel, S. B., Linden, P. F. & Youngs, D. L. 1999 Self-similarity and internal structure of turbulence induced by Rayleigh–Taylor instability. *J. Fluid Mech.* **399**, 1–48.

Dimonte, G. & Schneider, M. 2000 Density ratio dependence of Rayleigh–Taylor mixing for sustained and impulsive acceleration histories. *Phys. Fluids* **12**, 304–321.

Dimonte, G., Youngs, D. L., Dimits, A. *et al.* 2004 A comparative study of the turbulent Rayleigh–Taylor instability using high-resolution three-dimensional numerical simulations: the Alpha-Group collaboration. *Phys. Fluids* **16**, 1668–1693.

Fernando, H. J. S. 1991 Turbulent mixing in stratified fluids. *Annu. Rev. Fluid Mech.* **23**, 455–493.

Glimm, J., Zhang, Q. & Sharp, D. H. 1991 The renormalization group dynamics of chaotic mixing of unstable interfaces. *Phys. Fluids* A **3**, 1333–1335.

Higginson, R. C. 2000 Turbulence and mixing in a stratified fluid. PhD thesis, University of Cambridge.

Holford, J. M., Dalziel, S. B. & Youngs, D. L. 2003 Rayleigh–Taylor instability at a tilted interface in laboratory experiments and numerical simulations. *Laser Particle Beams* **21**, 419–423.

Holford, J. M. & Linden, P. F. 1999 Turbulent mixing in a stratified fluid**.** *Dyn. Atmos. Oceans* **30**, 173–198.

Kumagai, M. 1984 Turbulent buoyant convection from a source in a confined two-layer region. *J. Fluid Mech.* **147**, 105–131.

Linden, P. F. & Redondo, J. M. 1991 Molecular mixing in Rayleigh–Taylor instability. Part I. Global mixing. *Phys. Fluids* A **3**, 1269–1277.

Linden, P. F., Redondo, J. M. & Youngs, D. L. 1994 Molecular mixing in Rayleigh–Taylor instability. *J. Fluid Mech.* **265**, 97–124.

Nokes, R. I. 1988 On the entrainment rate across a density interface. *J. Fluid Mech.* **188**, 185–204.

Rayleigh, Lord 1900 Investigation of the character of the equilibrium of an incompressible heavy fluid of variable density. *The Scientific Papers of Lord Rayleigh*, vol. 2, pp.200–207. Cambridge University Press.

Read, K. I. 1984 Experimental investigation of turbulent mixing by Rayleigh–Taylor instability. *Physica* D **12**, 45–58.

Sharp, D. H. 1984 An overview of Rayleigh–Taylor instability. *Physica* D **12**, 3–18.

Snider, D. M. & Andrews, M. J. 1994 Rayleigh–Taylor and shear driven mixing with an unstable thermal stratification. *Phys. Fluids* **6**, 3324–3334.

Strang, E. & Fernando, H. J. S. 2001 Entrainment and mixing in stratified shear flows. *J. Fluid Mech.* **428**, 349–386.

Taylor, G. I. 1950 The instability of liquid surfaces when accelerated in a direction perpendicular to their planes. *Proc. R. Soc. Lond.* A **201**, 192–196.

Youngs, D. L. 1984 Numerical simulation of turbulent mixing by Rayleigh–Taylor instability. *Physica* D **12**, 32–44.

Youngs, D. L. 1991 Three-dimensional numerical simulation of turbulent mixing by Rayleigh–Taylor instability. *Phys. Fluids* A **3**, 1312–1320.